

A High-Fidelity 3D Simulator for Synthetic fNIRS Data Generation

Condell Eastmond
eastmc@rpi.edu

Niels Bracher
brachn@rpi.edu

Xavier Intes
intesx@rpi.edu

Stefan T. Radev
radevs@rpi.edu

June 1, 2026

Abstract

Functional near-infrared spectroscopy (fNIRS) provides a noninvasive window into brain activity by measuring task-related changes in oxygenated and deoxygenated hemoglobin in the cortex. A key advantage of fNIRS is its promise of use with mobile participants in complex, real-world environments, such as walking, sports, classroom learning, driving simulations, or social interactions. However, analyzing fNIRS data is challenging because of motion artifacts, physiological noise, and other confounding factors. This challenge is further compounded by the limited availability of annotated datasets, which hinders the development and validation of new analysis pipelines, particularly given the growing use of AI methods. Recognizing these challenges, we introduce a 3D fNIRS simulator that uses mesh-based Monte Carlo simulations to create physiologically realistic, full-head synthetic recordings with high spatiotemporal fidelity. Our simulator combines anatomically accurate sensitivity profiles with parameterized models of hemodynamic responses, systemic physiology, and nonsystematic artifacts. As a result, users can generate virtually unlimited labeled datasets for testing denoising algorithms, data augmentation, mechanistic modeling, or *in silico* experimentation. We validate the simulator using experimental fNIRS data from open-source finger-tapping, pain-assessment, and surgical-skill datasets and provide an open-source implementation to support reproducibility and broad adoption.

1 Introduction

Significant innovations in neuroimaging now enable us to visualize the brain in action (McDowell et al., 2013). In particular, functional near-infrared spectroscopy (fNIRS) utilizes near-infrared light to detect changes in cortical hemodynamic activity. Driven by advances in system miniaturization, wearability, and system sensitivity (Doherty et al., 2023), fNIRS is uniquely able to monitor and quantify fast, spatially-resolved brain activations of mobile participants in naturalistic environments over long periods of time (Gao et al., 2024; Pinti et al., 2020, 2018). Consequently, fNIRS has proven highly useful across various applications, including brain-computer interfaces (Naseer and Hong, 2015), monitoring of brain disorders (Rahman et al., 2020), and neurofeedback (Klein et al., 2024).

Despite its versatility, analyzing fNIRS data remains challenging. The primary goal is to extract cortical activation profiles from optical time series measurements that often contain features generated by numerous confounding factors, including motion artifacts, superficial signal contamination, and systemic physiological signals. These sources of noise obscure neural activity and complicate the accurate interpretation of measured hemodynamic responses. As a result, a wide range of refined analysis pipelines has been proposed; however, the field still lacks standardization and a universally accepted best practice (Yücel et al., 2025). This fragmentation has also contributed to a scarcity of large, annotated datasets for cross-validation and for

supporting the development of next-generation analysis pipelines, particularly those relying on AI (Doherty et al., 2023; Eastmond et al., 2022).

Herein, we argue that a high-fidelity fNIRS simulator can address these issues by providing access to flexible and controllable ground-truth data across different experimental configurations. Such a simulator would enable systematic benchmarking of signal processing algorithms using realistic ground-truths, while also providing a data augmentation pipeline for data-hungry AI models. In addition, it could support simulation-based inference approaches that link neural time series to mechanistic models of brain activity (Tolley et al., 2024). Moreover, a full-head simulator could accelerate experimental design by allowing researchers to virtually prototype optode configurations and predict signal quality prior to conducting costly *in vivo* experiments.

There are two general approaches to generating synthetic fNIRS data, each with distinct advantages and limitations. Recent advances in deep learning have enabled *data-driven methods*, which train generative neural networks (e.g., Generative Adversarial Networks; GANs, Goodfellow et al., 2014) to learn the statistical structure of observed data and generate realistic synthetic samples (Rasheed et al., 2021; Nagasawa et al., 2020; Wickramaratne and Mahmud, 2021). For example, Nagasawa et al. (2020) used a GAN to augment the training data of a neural classifier with synthetic fNIRS time series, resulting in an accuracy gain of around 30%. Generative AI approaches can capture complex patterns directly from data but often require large training annotated datasets and may lack interpretability or physiological grounding. Another data-driven approach involves using resting-state datasets seeded with synthetic HRFs and motion artifacts (Middell et al., 2026). While such approaches can produce realistic synthetic data, they are strictly limited by the quantity of experimental data present.

On the other hand, *theory-driven* (or first-principles) data generators rely on biophysically detailed forward models whose parameters have a direct mechanistic interpretation (Tolley et al., 2024). These theory-driven approaches have been used since the inception of fNIRS and have substantially benefited from increasingly accurate models of light propagation in complex biological tissues. For example, Liu et al. (2022) employed a layered slab model of head tissue to generate synthetic fNIRS data for validating a deep learning-based filtering method. However, this approach was limited by its simplified anatomical representation and required extensive domain knowledge, as well as labor-intensive manual tuning of numerous parameters to match the characteristics of individual experimental datasets. Moreover, many theory-driven models struggle to accurately capture spatiotemporal dynamics across the complex geometry of the human head (Tran et al., 2020), or do not attempt to do so at all, and instead rely on simplified single-channel simulations (Leamy et al., 2011).

In this work, we present a forward model that addresses the key limitations of existing theory-driven fNIRS simulators. Specifically, we introduce the first 3D fNIRS simulator that preserves spatiotemporal information across hemodynamic responses, systemic physiological signals, and nonsystematic artifacts by incorporating these components into a mesh-based Monte Carlo (MMC) light propagation forward model (Fang, 2010). At a high level, our approach estimates anatomically accurate Jacobians that characterize the sensitivity of all source–detector pairs to changes in optical absorption throughout the imaged volume (i.e., the full head) (Yao et al., 2018). Crucially, our approach can model spatiotemporal variations in optical absorption arising from systemic physiological processes (Hocke et al., 2018) (e.g., cardiac and respiratory activity, Mayer waves), measurement artifacts (e.g., baseline shifts, spikes, and channel dropout), and hemodynamic response functions (HRFs) driven by local neuronal activity.

In the following sections, we describe the mathematical foundations of our simulator and detail its

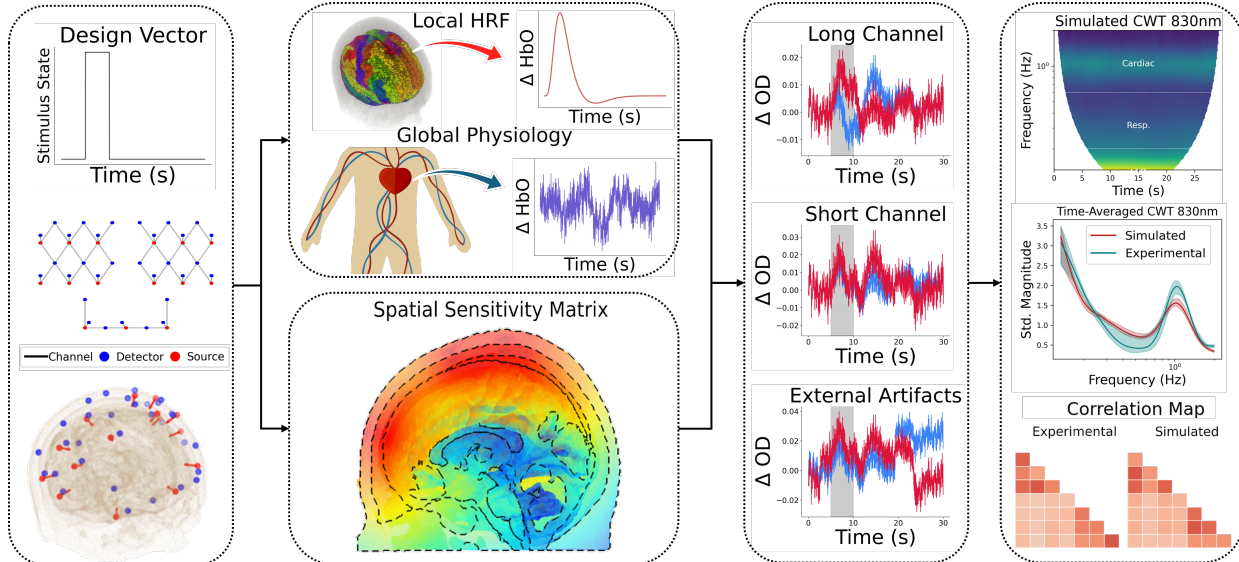


Figure 1: Graphical overview of the proposed framework for simulating high-quality multichannel fNIRS data. Starting from an experimental design and optode montage (*left*), the simulator combines task-evoked cortical responses, global physiological fluctuations, and external artifacts with a spatial sensitivity matrix derived from light-transport simulations (*middle*). These components are projected to channel-level changes in optical density (OD), producing synthetic long- and short-channel fNIRS time series (*middle-right*). The simulated data can be compared with empirical recordings using global and local metrics, such as time-frequency maps, time-averaged spectral profiles, or inter-channel correlation maps (*right*).

parameter configurations. We then validate both low- and high-level spatiotemporal signal characteristics of the simulated data against experimental fNIRS measurements from publicly annotated datasets. The proposed 3D fNIRS simulator is released as open-source software to ensure reproducibility and enable users to perform customized simulations. Figure 1 provides an overview of our proposed simulation framework.

2 Model

The following sections introduce our multi-component forward model for generating synthetic fNIRS time series and establish the relationship between the forward model’s parameters, denoted collectively as $\theta \in \Theta$ (for an overview see Table 1), and the time-dependent vector of intensities, denoted as $\phi_1(t; \theta) \in \mathbb{R}^C$. We start by introducing the Rytov approximation (O’Leary, 1996) to generate synthetic intensities $\phi_1(t; \theta)$ (see Section 2.1), using both a baseline intensity ϕ_0 and the sensitivity matrix \mathbf{J} , which are computed via MMC simulations (see Section 2.2). This approach reproduces the classical block design protocol that is prevalent in fNIRS studies (Luke et al., 2021a; Pinti et al., 2019). We then introduce the parameterization of the model which serves as the foundation for generating synthetic training data (see Section 2.3). Lastly, we introduce a variety of external artifacts to more realistically model fNIRS data (see Section 2.4). All model parameters and distributions introduced in the following are detailed in Appendix B.

Parameter	Symbol	Meaning	Description
θ_C	$\omega = (\omega_1, \dots, \omega_L)$	HRF widths	Widths of Hemodynamic Response Functions.
	$\tau = (\tau_1, \dots, \tau_L)$	HRF times to peak	Times from onset of stimulus to peak of HRF.
	$\kappa = (\kappa_1, \dots, \kappa_L)$	HRF amplitudes	Magnitude of HRF peaks.
	$\xi = (\xi_1, \dots, \xi_L)$	HRF HbO weights	Relative concentration change of HbO to HbR.
	η	Power offset	Constant signal offset in PSD; can be thought of as a global white noise contribution.
	$\zeta = (\zeta_1, \zeta_2)$	Systemic physiology weights	Scaling factor of systemic physiology time series signal for each wavelength.
θ_P	$\alpha = (\alpha_1, \alpha_2, \alpha_3)$	Relative amplitudes (Mayer waves, Respiratory, Cardiac)	Relative amplitude of Gaussian pulse to all systemic physiological contributions in the power spectral density; each α models an individual systemic physiological contribution to fNIRS signals.
	$\nu = (\nu_1, \nu_2, \nu_3)$	Central peak frequencies (Mayer waves, Respiratory, Cardiac)	Central frequency of Gaussian pulses in the power spectral density; each ν models an individual systemic physiological contribution to fNIRS signals.
	ρ	Aperiodic slope	Slope of the aperiodic $1/f^\rho$ exponential frequency component in the power spectral density.

Table 1: Overview of the simulation parameters $\theta = (\theta_C, \theta_P)$ associated with changes in absorption $\delta\mu_a$. The parameters are categorized into two groups: θ_C for cortical activation and θ_P for systemic physiology. L denotes the number of active regions.

2.1 Theoretical Foundation

fNIRS exploits the relative transparency of biological tissue in the near-infrared wavelength range (650 – 950) nm, where measured fluctuations in light absorption can be linked to hemodynamic variations within the probed tissue volume (Scholkmann et al., 2014). Positioning sources and detectors a few centimeters apart on the scalp enables light to penetrate several centimeters into the tissue, allowing measurements of cortical activity through changes in local hemodynamics associated with neuronal activation. By probing the tissue at multiple wavelengths, fNIRS performs spectroscopic measurements that allow discrimination between oxygenated and deoxygenated hemoglobin, enabling characterization of their spatiotemporal variations.

In practice, measurements typically follow block-design protocols, in which a rest period precedes a task or activity period. This design facilitates fNIRS data processing by providing a baseline measurement during rest and enabling analysis of task-related changes in hemoglobin concentrations, such as variations in oxygenated and deoxygenated hemoglobin during the activity period. Technically, this involves analyzing relative changes between a baseline (unperturbed) detected intensity ϕ_0 (rest) and a perturbed intensity $\phi_1(t)$ (task).

We formulate the simulation of intensity variations using the Rytov approximation. This model, widely used in diffuse optical tomography, relates changes in detected intensity to local variations in the absorption coefficient $\delta\mu_a(t; \theta)$ through the sensitivity matrix \mathbf{J} (O’Leary, 1996) (see Section 2.2). Let \mathcal{F} denote the forward operator (diffusion solver or Monte Carlo estimator) that maps discretized optical property fields to predicted measurements. After discretizing the domain into M mesh nodes, we represent absorption and scattering as vectors $\mu_a, \mu_s \in \mathbb{R}^M$ and define $\phi = \mathcal{F}(\mu_a, \mu_s) \in \mathbb{R}^D$ as the vector of detector measurements.

The Rytov approximation linearizes $\log \phi$ with respect to small perturbations in the absorption coefficient μ_a and scattering coefficient μ_s around a baseline (μ_a^0, μ_s^0) :

$$\log \phi(\mu_a, \mu_s) \approx \log \phi(\mu_a^0, \mu_s^0) + \left. \frac{\partial \log \phi}{\partial \mu_a} \right|_{\mu_a^0} \delta \mu_a + \left. \frac{\partial \log \phi}{\partial \mu_s} \right|_{\mu_s^0} \delta \mu_s. \quad (1)$$

As customary in the field of fNIRS, scattering is kept constant (i.e., $\delta \mu_s \approx 0$). Explicating the dependence of $\delta \mu_a$ on the tunable parameters θ yields the standard Rytov formulation:

$$\log \left(\frac{\phi_1(t; \theta)}{\phi_0} \right) \approx \mathbf{J} \delta \mu_a(t; \theta), \quad (2)$$

where $\phi_0 \equiv \phi(\mu_a^0, \mu_s^0)$ is the unperturbed intensity, $\phi_1(t; \theta) \equiv \phi(\mu_a, \mu_s)$ the perturbed intensity, and \mathbf{J} is the Jacobian of $\log \phi$ with respect to μ_a evaluated at μ_a^0 . Rearranging gives a direct expression for the predicted intensity:

$$\phi_1(t; \theta) \approx \phi_0 \exp(\mathbf{J} \delta \mu_a(t; \theta)), \quad (3)$$

which forms the basis of our simulation model. From this simulated intensity, we compute the change in optical density (ΔOD) by log-normalizing with respect to the average baseline intensity over a pre-stimulus period $\bar{\phi}_{\text{base}}$:

$$\Delta OD(t; \theta) = \log(\bar{\phi}_{\text{base}}) - \log(\phi_1(t; \theta)), \quad (4)$$

where

$$\bar{\phi}_{\text{base}} = \frac{1}{T_{\text{base}}} \int_0^{T_{\text{base}}} \phi_1(t; \theta) dt \quad (5)$$

is the average intensity during the baseline window of length T_{base} . Of note, $\bar{\phi}_{\text{base}}$ is computed as the mean pre-stimulus intensity for each channel and is different from the simulated unperturbed measurement vector ϕ_0 , which is generated via MMC. Using ΔOD time series enhances comparability across channels and subjects by providing a measurement of light attenuation instead of the total amount of detected light (Delpy et al., 1988).

2.2 Generating the Sensitivity Matrix

To model relative changes between the baseline detected intensity ϕ_0 (rest) and a perturbed intensity $\phi_1(t)$ (task) in measured intensity, light propagation models can be employed (Dehghani et al., 2009; Fang, 2010). In this context, Monte Carlo methods are widely regarded as the most accurate approach for modeling photon transport in complex biological tissues across a broad range of optical properties and measurement configurations. However, these methods are often computationally expensive, particularly when simulating deep tissue propagation, which requires large numbers of photon packets, or when repeated simulations are needed (Chen and Intes, 2011).

To address this challenge, we leverage the Mesh-based Monte Carlo toolbox (MMC; Fang, 2010), which enables efficient computation of three-dimensional tissue sensitivity profiles \mathbf{J} of measured intensity ϕ_1 to changes in the absorption coefficient μ_a (Yao et al., 2018; Nizam et al., 2022). MMC simulates light transport through a tetrahedral mesh of biological tissue, providing a flexible framework for generating subject- or atlas-based forward models. Its practical applicability has improved significantly in recent years due to advances in computational power and GPU parallelization (Fang and Yan, 2019).

The inputs to the MMC simulations consist of three main components: anatomical information, exper-

Dimension	Description
C	Number of channels
R	Number of sources
D	Number of detectors
L	Number of active cortical regions
M	Number of mesh points

Table 2: Overview of number of dimensions of key quantities in the forward model.

imental configuration, and tissue-specific optical properties. First, for the anatomical model, we followed the procedure described by Zimeo Morais et al. (2018) to generate a high-resolution segmented tetrahedral brain mesh based on the Colin27 atlas (Holmes et al., 1998). We further divided this mesh into functional cortical regions by using the SPM12 toolbox (Friston, 2003) to coregister the segmented tissue map to the Automated Anatomical Labeling Atlas 3 (AAL3) (Rolls et al., 2020).

Second, the experimental configuration is defined by the optode montage (Figure 4). The montage comprises both long- and short-separation channels, where each channel corresponds to a source-detector pair. Short-separation channels are primarily sensitive to superficial/systemic signals, whereas long-separation channels are more sensitive to deeper, cortical activations, although typically at the cost of a lower signal-to-noise ratio (SNR). Different montages are used for the different experimental protocols described in Section 3.1 (Yücel et al., 2015a; Kamat et al., 2023).

Before running the simulations, the digitized probe geometry is registered to the tetrahedral head mesh. The 3D optode coordinates are first rotated into RAS (Right, Anterior, Superior) orientation and then projected onto the mesh surface using the iterative closest point (ICP) algorithm (Besl and McKay, 1992). The source directions are assumed to point from the optode locations toward the centroid of the mesh. The optodes are embedded one mean free path beneath the mesh surface (Fang, 2010).

Third, the tissue-specific optical properties used in the simulations include the absorption coefficient μ_a , the scattering coefficient μ_s , the anisotropy factor g , and the refractive index m . Their values were obtained from existing literature and are summarized in Table A3.

Simulating photon propagation through the mesh yields the detected baseline fluence ϕ_0 , as well as the spatial distribution of fluence inside the brain mesh in the form of a Green’s function, assuming a unit-intensity light source (Fang and Boas, 2009). We then compute the sensitivity matrix for all possible source-detector pairs $\mathbf{J}^{(\text{all})} \in \mathbb{R}^{RD \times M}$, using the adjoint method (Yao et al., 2018). An overview of the dimensionality of key quantities is provided in Table 2.

More specifically, we first run R simulations, one for each source, to obtain the Green’s function $\mathbf{G}^R \in \mathbb{R}^{R \times M}$, which describes the sensitivity of each mesh point to each source. These simulations also provide the detected fluence for all source-detector pairs, denoted by $\mathbf{G}^{RD} \in \mathbb{R}^{RD}$. We then use the reciprocity of light transport and run D additional simulations, placing a virtual source at each detector. This yields $\mathbf{G}^D \in \mathbb{R}^{D \times M}$, which describes the sensitivity of each mesh point to each detector.

The row corresponding to the i th source-detector pair of the full Jacobian, $\mathbf{J}_i^{(\text{all})}$, is calculated as

$$\mathbf{J}_i^{(\text{all})} = \frac{\mathbf{G}_r^R \odot \mathbf{G}_d^D}{\mathbf{G}_i^{RD}}, \quad (6)$$

where i indexes a specific source-detector pair, composed of source r and detector d . Here, \mathbf{G}_r^R denotes the row of \mathbf{G}^R corresponding to source r , and \mathbf{G}_d^D denotes the row of \mathbf{G}^D corresponding to detector d . The

symbol \odot denotes elementwise multiplication between the two vectors.

The full Jacobian $\mathbf{J}^{(\text{all})}$ contains sensitivities for all possible source-detector combinations at all mesh points. However, only a subset of these combinations corresponds to actual measurement channels in the experimental montage. Therefore, after constructing $\mathbf{J}^{(\text{all})}$, we retain only the rows corresponding to the source-detector pairs used in the experiment. The resulting sensitivity matrix is denoted by $\mathbf{J} \in \mathbb{R}^{C \times M}$, where $C \leq RD$ is the number of measured channels and M is the mesh size.

2.3 Modeling Change in Absorption

The total change in absorption coefficient for wavelength λ across all M mesh points is modeled as a weighted sum of cortical and systemic contributions that are parameterized via $\boldsymbol{\theta}$ (see Table 1):

$$\delta\mu_a(t, \lambda; \boldsymbol{\theta}) = \delta\mu_C(t, \lambda; \boldsymbol{\theta}_C) + \sqrt{\frac{\zeta_\lambda}{1 - \zeta_\lambda}} \delta\mu_P(t; \boldsymbol{\theta}_P), \quad (7)$$

where $\delta\mu_C(t, \lambda; \boldsymbol{\theta}_C)$ is the absorption change due to *cortical hemodynamic activity*, and $\delta\mu_P(t; \boldsymbol{\theta}_P)$ represents absorption changes caused by *systemic physiology* (e.g., heart rate, respiration, blood pressure). The wavelength-dependent parameter $\zeta_\lambda \in [0, 1]$ can be thought of as the fraction (percentage) of signal variance attributable to physiological factors (Aarabi and Huppert, 2016). To ensure that systemic fluctuations are appropriately scaled relative to the cortical signal, we first normalize the physiological noise time series by its own standard deviation and rescale it to match the standard deviation of the cortical activation:

$$\delta\tilde{\mu}_P(t; \boldsymbol{\theta}_P) = \frac{\sigma_C}{\sigma_P} \delta\mu_P(t; \boldsymbol{\theta}_P), \quad (8)$$

where $\sigma_C = \text{std}(\delta\mu_C)$ and $\sigma_P = \text{std}(\delta\mu_P)$. This prevents one component from dominating solely due to scale differences (e.g., if systemic physiology has much higher variance than cortical activation) and makes the ζ_λ parameter interpretable.

2.3.1 Cortical Hemodynamic Activity

The cortical contribution (see Figure 2) is modeled as a linear combination of spatial activity maps and time-varying cortical responses:

$$\delta\mu_C(t, \lambda; \boldsymbol{\theta}_C) = \mathbf{A}(\mathbf{s}(\lambda; \boldsymbol{\theta}_C) \odot \mathbf{c}(t; \boldsymbol{\theta}_C)), \quad (9)$$

where $\mathbf{A} \in \mathbb{R}^{M \times L}$ is a matrix encoding spatial locations of cortical activations, $\mathbf{c}(t; \boldsymbol{\theta}_C) \in \mathbb{R}^L$ describes their temporal amplitudes, and $\mathbf{s}(\lambda; \boldsymbol{\theta}_C) \in \mathbb{R}^L$ is a vector of wavelength-dependent scaling factors based on the molar extinction coefficients of oxy- and deoxygenated hemoglobin $\epsilon(\lambda)$ (Wray et al., 1988). Each column of \mathbf{A} corresponds to a binary activation map of a pre-selected region where it is assumed cortex activation will occur. These active regions are spatially defined via the functional cortical map and are based on AAL3 segmentation (see Section 2.2). The scaling factors are computed as

$$\mathbf{s}(\lambda; \boldsymbol{\theta}_C) = \boldsymbol{\xi} \epsilon_{\text{HbO}}(\lambda) - (\mathbf{1} - \boldsymbol{\xi}) \epsilon_{\text{HbR}}(\lambda), \quad (10)$$

where $\boldsymbol{\xi} \in \boldsymbol{\theta}_C$ controls the relative weight of change in oxyhemoglobin (HbO) relative to the change in deoxyhemoglobin (HbR). Finally, the temporal response $\mathbf{c}(t; \boldsymbol{\theta}_C)$ is modeled by convolving the experimental

Physiological Origin	Frequency Band [Hz]	Reference
Cardiac Activity	.60 – 2.5	Leamy et al. (2011); Hocke et al. (2018); Nguyen et al. (2018)
Respiratory Activity	.20 – .60	Hocke et al. (2018); Nguyen et al. (2018)
Blood Pressure Fluctuations (Mayer Waves)	.06 – .14	Nguyen et al. (2018); Luke et al. (2021b)

Table 3: Systemic physiology frequency bands used to construct informative priors over the systemic physiology parameters of our simulator.

design vector $x(t)$ with a parametric hemodynamic response function (HRF) $h(t, \boldsymbol{\theta}_{C,\ell})$:

$$c_\ell(t; \boldsymbol{\theta}_{C,\ell}) = (x * h_\ell)(t; \boldsymbol{\theta}_{C,\ell}), \quad \ell = 1, \dots, L, \quad (11)$$

where $\boldsymbol{\theta}_{C,\ell}$ denotes the set of parameters governing the HRF’s shape at cortical activation ℓ .

Hemodynamic Response Function The HRF $h_\ell(t)$ models the stereotypical shape of the cortical response using the canonical double-gamma HRF (Lindquist et al., 2009):

$$h(t; \kappa, \tau, \omega) = \kappa \left(\frac{t^{\tau-1} \omega^\tau e^{-\omega t}}{\Gamma(\tau)} - \frac{1}{6} \frac{t^{\tau+\tau_0-1} \omega^{\tau+\tau_0} e^{-\omega t}}{\Gamma(\tau + \tau_0)} \right), \quad (12)$$

where τ_0 fixes the delay between positive and undershoot peaks. An independent HRF is modeled for every cortical activation, with each cortical activation occurring at a selected region of the AAL3-segmented mesh ℓ , resulting in the parameter vector $(\kappa_\ell, \tau_\ell, \omega_\ell) \subset \boldsymbol{\theta}_{C,\ell}$, where κ_ℓ, τ_ℓ , and ω_ℓ refer to HRF amplitude, time to peak and width, respectively.

As shown in Lindquist et al. (2009) the addition of temporal and dispersion derivatives may improve HRF modeling. Our simulator allows for the optional inclusion of these derivatives in modeling the temporal response. The double gamma models implemented are the Glover canonical HRF model (Glover, 1999) and the SPM canonical HRF model (Lindquist et al., 2009). For all analysis in this paper, the SPM model is used.

Design Vector A binary time-dependent stimulus state $x(t) \in \{0, 1\}$ indicates when a subject is presented with an experimental event (1 = ON, 0 = OFF) based on the experimental task. For example, in a block-design finger-tapping task with 5 seconds of tapping and 20 seconds of rest (Yücel et al., 2015a), the design vector for a given trial would look like:

$$\mathbf{x} = [\underbrace{1, \dots, 1}_{5 \text{ s}}, \underbrace{0, \dots, 0}_{20 \text{ s}}]. \quad (13)$$

Thus, convolving the HRF of each active region with the design vector (Eq. 11) ensures that the simulated activation follows the timing of the experimental protocol (Section 3.1).

2.3.2 Systemic Physiology

We model changes in absorption due to systemic physiology $\delta\mu_P$ (see Figure 2) in the frequency domain, construct a complex-valued frequency spectrum, and subsequently transform it into the time domain via the

inverse Fourier transform (McSharry et al., 2003):

$$\delta\mu_P(t; \theta_P) = \mathcal{F}^{-1} [\delta M_P(f; \theta_P)], \quad (14)$$

where f denotes frequency, θ_P the set of systemic physiological parameters, and \mathcal{F}^{-1} the inverse Fourier transform. The complex frequency-domain representation δM_P is defined as

$$\delta M_P(f; \theta_P) = \sqrt{\text{PSD}(f; \theta_P) \frac{df}{2}} e^{j\beta(f)}, \quad (15)$$

where df is the frequency resolution (inversely proportional to the time-series length), j the imaginary unit, and $\beta(f) \sim \mathcal{U}[0, 2\pi)$ is a randomly sampled phase ensuring proper phase scrambling. The power spectral density (PSD) is modeled as the sum of an aperiodic $1/f$ component and periodic Gaussian peaks corresponding to physiological oscillations:

$$\text{PSD}(f; \theta_P) = \text{PSD}_{\text{aperiodic}}(f; \theta_P) + \text{PSD}_{\text{periodic}}(f; \theta_P). \quad (16)$$

The *aperiodic component* accounts for broadband background fluctuations and is modeled as a power-law ($1/f$) process with a low-frequency stabilizer:

$$\text{PSD}_{\text{aperiodic}}(f; \theta_P) = \frac{\eta}{(f + \tilde{f})^\rho} + u, \quad (17)$$

where η is the spectral power offset, ρ is the $1/f$ exponent controlling the slope, and $\tilde{f} > 0$ is a small stability constant that prevents divergence as $f \rightarrow 0$. The term $u \sim \mathcal{N}(0, \sigma_u^2)$ represents additive Gaussian noise with a small scale ($\sigma_u \approx 0.1$), which creates variability across frequency bins.

Differently, the *periodic component* models rhythmic oscillations in three characteristic frequency bands (e.g., cardiac, respiratory, and Mayer waves; see Table 3) as a mixture of Gaussian peaks:

$$\text{PSD}_{\text{periodic}}(f; \theta_P) = \sum_{b=1}^3 \frac{\alpha_b}{\sqrt{2\pi} \sigma_b} \exp \left[-\frac{1}{2} \left(\frac{f - \nu_b}{\sigma_b} \right)^2 \right], \quad (18)$$

where α_b is the amplitude, ν_b the central frequency, and $\sigma_b \in \{0.015, 0.02, 0.08\}$ the spectral width of each component. The values of σ_b are heuristically chosen and can be tuned to match subject-specific physiology.

2.4 External Artifact Generation

To generate synthetic data representative of artifacts commonly observed in fNIRS, we explicitly model motion artifacts (i.e., spikes and baseline shifts) and apply them to the simulated raw intensity time series $\phi_1(t; \theta) \in \mathbb{R}^C$ (Gao et al., 2022; Barker et al., 2013) (see Figure 2). Artifacts are generated independently for each channel and then combined.

Let $\psi_s(t) \in \mathbb{R}^C$ denote the spike artifact vector and $\psi_b(t) \in \mathbb{R}^C$ the baseline-shift artifact vector at time index t . The corrupted intensity is defined as

$$\tilde{\phi}_1(t; \theta) = \phi_1(t; \theta) + \text{diag}(\sigma(\phi_1(t; \theta))) \left(\psi_s(t) + \psi_b(t) \right), \quad (19)$$

where $\sigma(\phi_1(\cdot; \theta)) \in \mathbb{R}^C$ is the vector of channel-wise standard deviations of the raw intensity time series

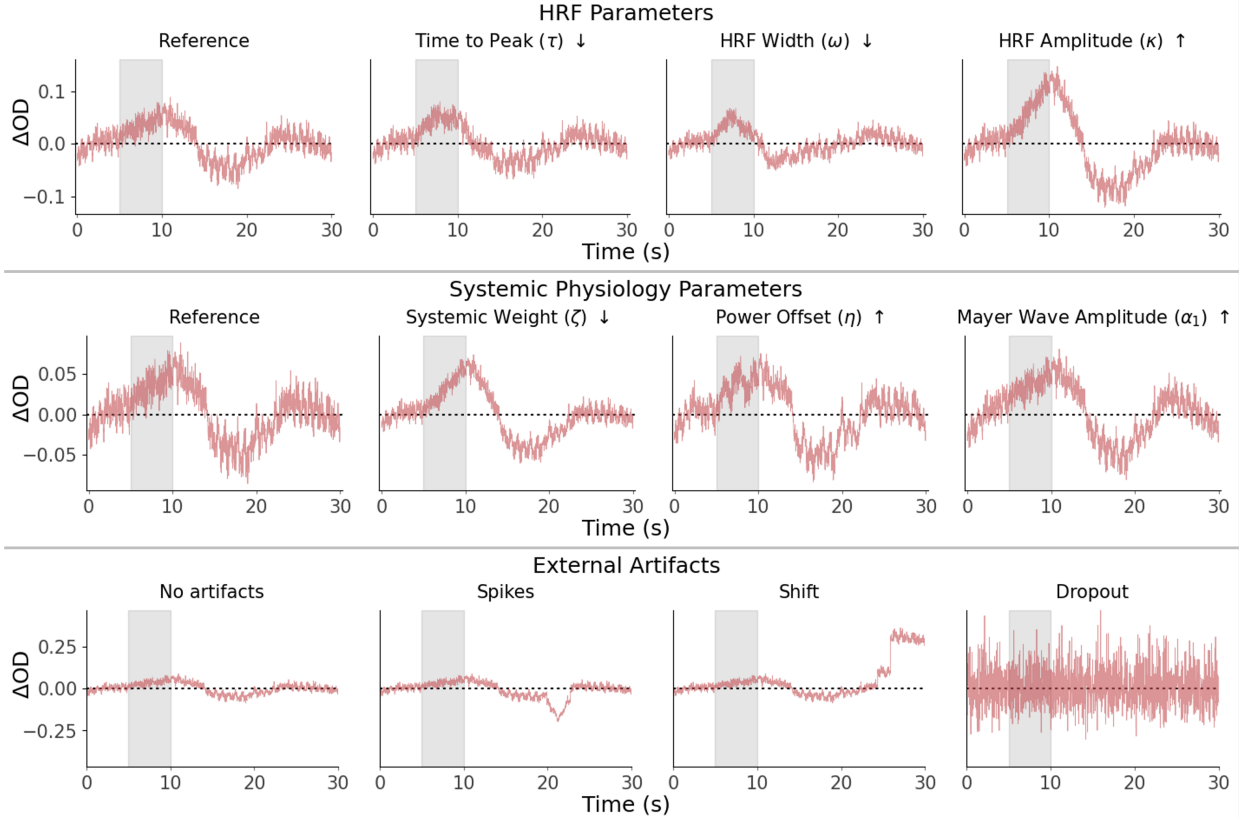


Figure 2: The impact of HRF parameters (*top*) systemic physiology parameters (*middle*) and external artifacts (*bottom*) on the change of optical density ΔOD over time for the 830 nm wavelength. The shaded region indicates the stimulus period.

(computed per channel over $t = 1, \dots, T$), and $\text{diag}(\cdot)$ converts it to a diagonal scaling matrix. This scaling expresses artifact magnitudes relative to each channel’s native intensity variability. To prevent unrealistically low (or negative) intensity values after corruption, we clip elementwise at a small heuristically chosen floor $u > 0$:

$$\tilde{\phi}_1(t; \theta) \leftarrow \max(\tilde{\phi}_1(t; \theta), u). \quad (20)$$

Spike Generation To simulate temporary optode displacements, we model spike artifacts as exponentially decaying pulses centered at randomly selected time points, independently for each channel. Let p_s denote the per-sample probability of a spike center, obtained from a per-second probability P_s via

$$p_s = \frac{P_s}{r}, \quad (21)$$

where r is again the sampling rate (Hz). For each channel $c \in \{1, \dots, C\}$ and time index $t \in \{1, \dots, T\}$, we define the random set of spike-center times in channel c as $\mathcal{T}_{s,c} = \{t : z_{t,c}^{(s)} = 1\}$, with $z_{t,c}^{(s)} \sim \text{Bernoulli}(p_s)$. For each $\tau \in \mathcal{T}_{s,c}$ we sample a half-width $w_{\tau,c}$ and signed amplitude $a_{\tau,c}$ as

$$w_{\tau,c} \sim \text{DiscreteUniform}(\lfloor r/4 \rfloor, \lfloor 2r \rfloor), \quad a_{\tau,c} \sim \text{Uniform}(-a_s/2, a_s/2), \quad (22)$$

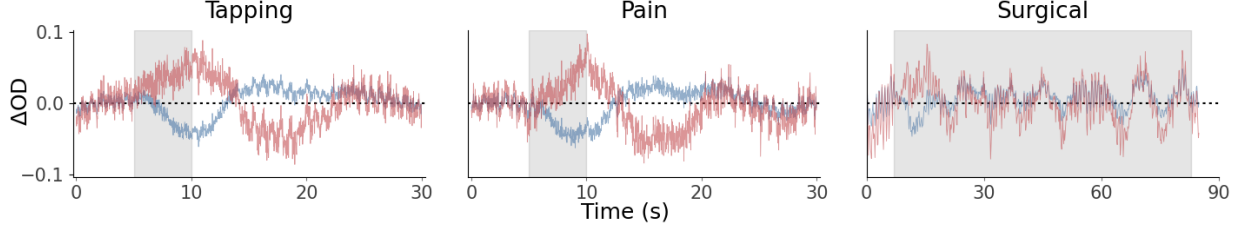


Figure 3: Simulated signals using the same set of parameters (sampled from Table A4) across different tasks. From left to right: finger tapping, pain assessment, and surgical skill assessment. The change in optical density ΔOD over time is shown for both wavelengths, 690 nm (blue) and 830 nm (red). The stimulus period is indicated by the gray shaded region.

with a heuristically determined scaling parameter $a_s > 0$. The sum of spike artifacts for channel c is described by the following:

$$\psi_{s,c}(t) = \sum_{\tau \in \mathcal{T}_{s,c}} a_{\tau,c} \exp\left(-\frac{|t - \tau|}{w_{\tau,c}}\right) \mathbb{I}\{|t - \tau| \leq w_{\tau,c}\}. \quad (23)$$

Stacking across channels gives the spike vector $\boldsymbol{\psi}_s(t) = (\psi_{s,1}(t), \dots, \psi_{s,C}(t))^\top$.

Baseline Shift Generation To simulate permanent changes in optode coupling, we model baseline shifts as step-like offsets with randomly selected onset times, independently for each channel. Let p_b denote the per-sample probability of a baseline-shift onset, obtained from a per-second probability P_b via

$$p_b = \frac{P_b}{r}, \quad (24)$$

where r is the sampling rate (Hz). For each channel $c \in \{1, \dots, C\}$ and time index $t \in \{1, \dots, T\}$, we define the (random) set of onset times in channel c as $\mathcal{T}_{b,c} = \{t : z_{t,c}^{(b)} = 1\}$, with $z_{t,c}^{(b)} \sim \text{Bernoulli}(p_b)$. For each $\tau \in \mathcal{T}_{b,c}$, we sample a signed step amplitude $a_{\tau,c} \sim \text{Uniform}(-a_b/2, a_b/2)$ with scaling parameter $a_b > 0$. Accordingly, the sum of baseline-shift artifacts for channel c is given by:

$$\psi_{b,c}(t) = \sum_{\tau \in \mathcal{T}_{b,c}} a_{\tau,c} \mathbb{I}\{t \geq \tau\}, \quad (25)$$

where stacking across channels gives the baseline-shift vector $\boldsymbol{\psi}_b(t) = (\psi_{b,1}(t), \dots, \psi_{b,C}(t))^\top$.

Channel Dropout Finally, to model channel dropout, we assume a random probability P_d (determined heuristically for each dataset) that any given channel is replaced by Gaussian noise with mean equal to that channel's mean and amplitude A_d . Due to the possibility of random noise producing negative intensity values, any noisy channel with a minimum below a heuristically determined threshold, u_d , is rescaled so that the channel mean remains unchanged while the minimum equals the threshold.

3 Materials and Methods

3.1 Experimental Data

The experimental data used to validate our simulator come from the publicly available finger-tapping and electrical pain assessment datasets (Yücel et al., 2015b) and the sham condition of the long-term tES surgical pattern cutting dataset (Kamat et al., 2023). For the surgical skill assessment dataset, we use trials between 30 and 98 seconds, since anything below 30 seconds is likely to be a mistake (e.g., a trigger pressed twice), and anything above 98 seconds is considered an outlier (based on the protocol design). Here, we use only the sham (control) condition to assess our proposed method’s ability to model differences in experimental hardware, subjects, and task duration. For ease of analysis, we crop all experimental and simulated trials to 30 seconds. Below, we provide brief descriptions of the experimental hardware, subjects, and protocols.

3.1.1 Hardware and Equipment

The finger tapping dataset used a continuous-wave 32-channel near-infrared spectrometer that delivered light at 690 nm and 830 nm (CW6 system, TechEn Inc., MA, USA). The experimental montage consisted of 11 sources, 16 long-separation detectors, and 11 short-separation detectors, with source-detector separations of approximately 3 cm and 0.8 cm for long- and short-separation channels, respectively. The probe covers the frontal cortex and portions of the somatosensory and motor areas across both hemispheres (Figure 4, *top left*).

The surgical skill assessment dataset used a continuous-wave near-infrared spectrometer that delivered light at 760 nm and 830 nm (NIRScout system, NIRx, Berlin, Germany). The experimental montage comprised 8 sources, 11 long-separation detectors, and 8 short-separation detectors, with source-detector separations of approximately 3 cm and 0.8 cm for the 28 long- and 8 short-separation channels, respectively. The probe covers the prefrontal cortex, primary motor cortex, and supplementary motor area across both hemispheres (Figure 4, *right*). Transcranial electrical stimulation (tES) was delivered via a StarStim device (StarStim, Neuroelectronics, Spain).

3.1.2 Subjects and Experimental Protocol

The finger tapping/electrical stimulus experimental sample consisted of 11 healthy, right-handed males (25 ± 5 years old) with no history of neurological trauma or psychiatric disorders. The subjects underwent a left-hand finger-tapping task, which involved a block design of 5 s of stimulus, followed by 25 s of rest, repeated 12 times for a total of 16 minutes, during which fNIRS recordings were taken. Example simulated trials for this dataset, along with a detailed list of model parameter distributions, are provided in Section B.2, with simulated example trial shown in Figure 3.

The surgical skill assessment sample consisted of 7 healthy, right-handed subjects with a mean age of 21 ± 1 . The surgical skill assessment task performed is the FLS pattern-cutting task, in which subjects attempted to cut a pre-marked circle from a gauze sheet within an FLS box simulator (Kamat et al., 2023). Before beginning the training, subjects underwent a pre-training period that began with a tutorial video and was followed by a practice trial of the pattern-cutting task. For the following 10 training days, subjects underwent sham tES, in which a transcranial electrical stimulation ramped up from 0 to 1 mA over 30s, then ramped back down to 0 mA at both the beginning and end of a 10-minute stimulation period. Afterward, subjects performed repeated trials of the pattern-cutting task for 30 minutes, with 30-second rest intervals

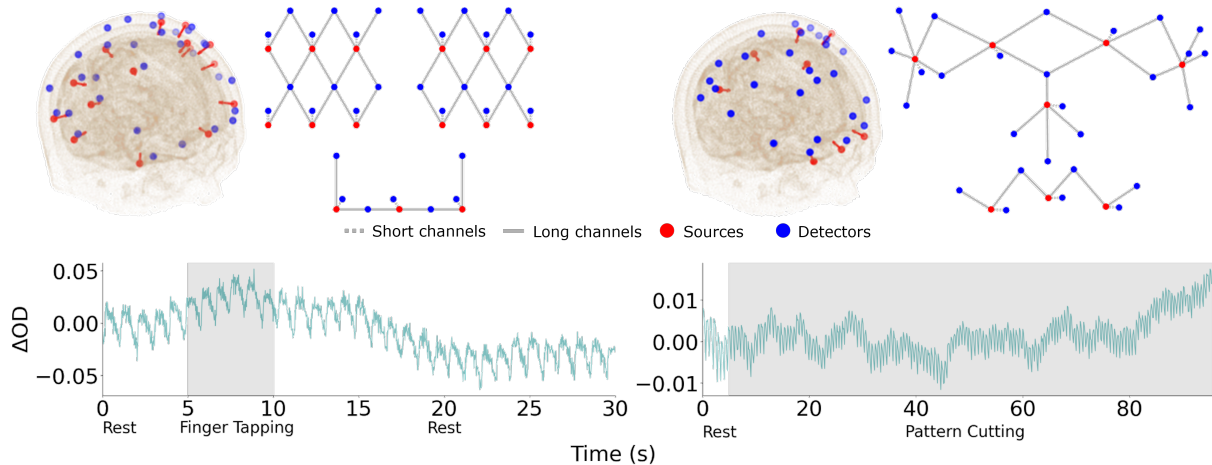


Figure 4: 2D layouts and 3D projections of the experimental montages (*top*) for the finger tapping and pain assessment (*left*; Yücel et al., 2015b), and surgical skill assessment (*right*; Kamat et al., 2023) datasets. An example channel with measured change of optical densities ΔOD with shaded stimulus periods (*bottom*) is shown for each of the data sets.

between trials. This resulted in 3-10 repetitions of pattern cutting per training period, with the training periods occurring on 10 consecutive days after the introductory day. On the day following the final training day, subjects performed a post-test consisting of 3 trials of the pattern-cutting FLS task. 30 seconds after the final post-test trial, subjects performed a transfer learning task, where they removed a marked circle from a layer of *ex vivo* porcine abdominal tissue. Fourteen days after this post-test, subjects performed a retention test identical to the post-test, consisting of 3 pattern-cutting trial repetitions followed by 1 transfer-learning trial. Example simulated trials for this dataset, along with a detailed list of model parameter distributions, are provided in Section B.3 with simulated example trial shown in Figure 3.

3.2 Data Denoising

To isolate cortical activity in both the simulated and experimental signals, we apply a denoising pipeline to the change in optical density of each signal. To remove high-frequency physiological contributions and baseline drift, a third-order Butterworth bandpass filter is applied with a 0.01-0.14 Hz bandwidth. Any remaining motion artifacts are removed from the data via the hybrid spline interpolation Savitzky-Golay filter (Jahani et al., 2018), implemented in the Homer3 toolbox (Huppert et al., 2009). The same denoising pipeline was applied to both experimental and simulated data. After denoising, the data were converted to ΔHbO using the modified Beer-Lambert law.

3.3 Model Comparison

To evaluate the proposed Jacobian-based simulator, we compare it against two alternative simulation approaches. The first is an autoregressive (AR) simulator implemented in existing fNIRS analysis toolboxes. The second is a Jacobian-free version of our simulator that retains the same generative components but omits the Jacobian-based spatial projection. These comparisons are used to assess whether the proposed model improves the spatial and temporal structure of the simulated measurements beyond existing or simplified

alternatives.

3.3.1 Autoregressive Simulator

As a baseline comparison, we use the autoregressive (AR) fNIRS simulator (Santosa et al., 2018) implemented in the MNE-NIRS toolbox (Luke et al., 2021a). This simulator generates synthetic optical density data by combining task-evoked hemodynamic responses with temporally autocorrelated noise. To match the experimental recordings, the cross-channel covariance matrix used to simulate the data is estimated from the experimental data, and the standard deviations of the simulated optical densities are scaled to match those of the experimental optical densities.

3.3.2 Jacobian-Free Simulator

To test the claim that the sensitivity matrix is necessary to adequately represent the spatial relationships among local hemodynamic responses, we compare our simulator with an ablated version that does not rely on the Jacobian \mathbf{J} to generate synthetic fNIRS signals. Instead of projecting $\delta\mu_a(t; \boldsymbol{\theta})$ spatially via the Jacobian (Equation 2), we alternatively multiply the cortical activations $\mathbf{c}(t; \boldsymbol{\theta}_C)$ with an $L \times C$ detector-measurement channel matrix \mathbf{D}_C to project the cortical activity to measurement channel space. \mathbf{D}_C is initialized as a sparse matrix of ones, where each activation corresponds to a measurement channel and 0 everywhere else. To simulate channel crosstalk, uniform noise ranging from 0 to 0.1 is added to the matrix, and each column is normalized to 1. The Jacobian-free simulator then models the change in detected intensity as a weighted sum of cortical and systemic physiology components as in Equation 7:

$$\delta\mu_a(t; \lambda, \boldsymbol{\theta}) = (1 - \zeta_\lambda) g_1 \mathbf{D}_C \delta\mu_C(t, \lambda; \boldsymbol{\theta}_C) + \zeta_\lambda g_2 \delta\mu_P(t; \boldsymbol{\theta}_S), \quad (26)$$

where ζ_λ controls the relative contributions. The heuristic scaling factors are set to $g_1 = 500$ and $g_2 = 1500$. External artifact generation is identical to our full simulator.

3.4 Validation

3.4.1 Model Ablation

To assess the contribution of each model component described in Section 2, we perform an additive ablation study. Starting from the cortical activity model alone, we progressively add systemic physiology, external artifacts, and the full set of model components. Specifically, we generate synthetic finger-tapping data under four conditions using the same input model parameters: (1) cortical activity only; (2) cortical activity with systemic physiology; (3) cortical activity with systemic physiology and external artifacts; and (4) the full model.

We then examine how each added component contributes to the cross-channel spatiotemporal structure of the simulated measurements by comparison with the real measurements. For each condition, we estimate the correlation matrix across selected long-separation channels located over the region of interest (ROI), here the right primary motor cortex (M1) during a left-hand finger-tapping task. To illustrate the spatially localized effect of the HRF, we also include a distant channel over the left somatosensory cortex. Correlation matrices are computed for each trial, averaged across trials, and compared across ablation conditions.

3.4.2 Local HRF Comparison

To isolate the cortical hemodynamic response, we use the denoising pipeline described above on both experimental and simulated data with external artifacts. To assess how local spatiotemporal information is preserved across channels, we then calculate the cross-channel correlation matrix of the denoised ΔHbO signal for the long-separation channels above the ROI. We then compare the correlation matrices, averaged across trials, to obtain a single average correlation matrix for each simulated and experimental dataset. Using the structural similarity index metric (SSIM), we compare how well each simulator preserves spatiotemporal information across the average cross-channel correlation matrix. Because the finger tapping task involves a left-handed finger tapping task, channels above the right M1 region of the cortex are selected for an ROI. For the bimanual surgical training task used for the surgical skill assessment, channels above the left and right M1 are used as the ROI.

3.4.3 Spectral Analysis

Finally, we compare the systemic physiology in the experimental and synthetic data using spectral features from short-separation channels. Optical density data are first standardized independently for each channel. We then compute the continuous wavelet transform (CWT) for all short-separation channels and average the spectra across channels and trials. The CWT is computed using a complex Morlet wavelet with a center frequency of 1.5 and a bandwidth of 1.0. As in Reddy et al. (2021), we use the time-averaged CWT as the spectral summary for each condition. Similarity between experimental and synthetic data is quantified using the R^2 value between their time-averaged CWT spectra.

We omit a separate comparison for the Jacobian-free model because systemic physiology is generated identically in the Jacobian-free and full models. In the surgical skill assessment dataset, trial durations vary; therefore, each trial is cropped to the first 25 seconds for spectral analysis.

4 Results

The following sections demonstrate the ability of our model to generate high-quality synthetic data with realistic local and global structure.

4.1 Ablation Study

The ablation results follow the expected component-wise behavior (Figure 5, top). The full simulator best reproduces the heterogeneous cross-channel structure observed in the experimental data, with stronger correlations among channels over the motor ROI and weaker, less uniform correlations elsewhere. When external artifacts are removed, the simulated correlations become overly regular, indicating that these components are important for breaking the otherwise idealized channel structure. The systemic physiology component produces broadly shared fluctuations and therefore induces high correlations across channels, consistent with its global nature. In contrast, the HRF-only condition induces correlations mainly among channels above the activated right M1 region, while the distant channel remains largely uncorrelated.

Notably, channel S11-D11, which lies near the edge of the ROI, receives a relatively weaker local HRF contribution than channels located closer to the center of the ROI. This reduced HRF amplitude does not necessarily appear as a lower correlation in the HRF-only condition, since correlation is insensitive to absolute signal scale. In the component mixture (Equation 7), however, the weaker local HRF contribution increases

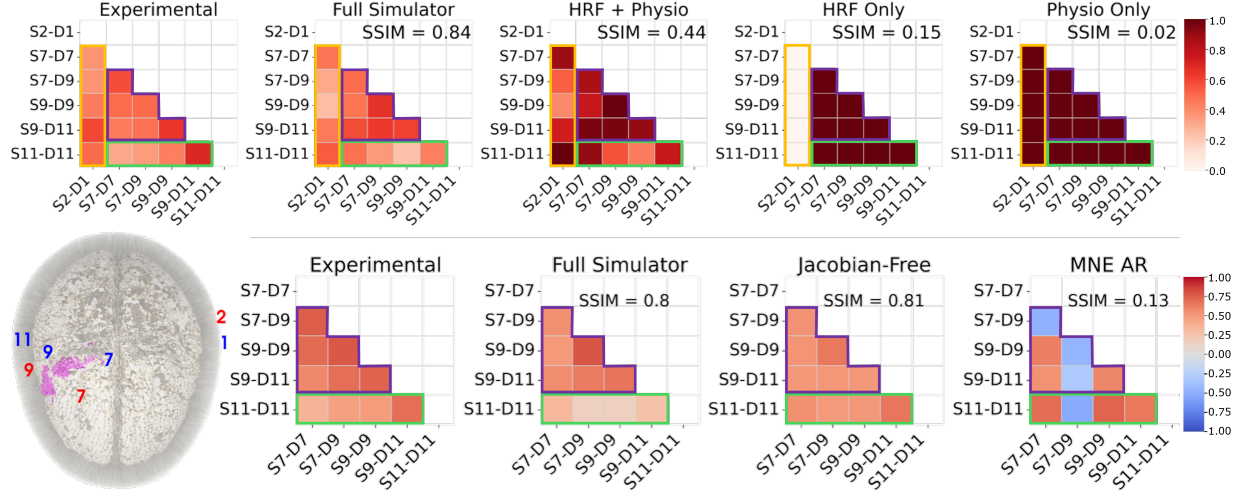


Figure 5: *Top*: Mean correlation matrices of change in optical density for empirical finger tapping data and simulated data along with data generated with ablated versions of the simulator. Only channels directly above the ROI (*purple*), a channel on the edge of the ROI (*green*) and an example distant channel (*yellow*) are shown here. *Bottom-left*: Diagram of head mesh with active region (right primary motor cortex) highlighted in pink with relevant source (*red*) and detector (*blue*) positions. *Bottom*: Mean correlation matrices for ΔHbO of channels above the ROI for the experimental data, the full simulator, and the two benchmark simulators.

the relative influence of the global systemic component, consistent with the elevated correlation between S11-D11 and the distant S2-D1 channel in the “HRF+Physio” panel.

Together, these trends show that the ablation isolates the expected spatial roles of the simulator components: localized cortical hemodynamics, global systemic physiology, and artifact variability that makes the full simulation more similar to experimental measurements.

4.2 Cortical Activity

For the finger-tapping dataset, the experimental ΔHbO correlation matrix over right M1 shows the expected spatial structure (Figure 5, *bottom*). Channels that are spatially close (e.g., channels S7-D9 and S9-D9) tend to exhibit stronger correlations than more separated channel pairs (e.g., channels S7-D7 and S11-D11). Furthermore, channels with reduced overlap with the ROI (e.g. channel S11-D11) demonstrate reduced correlation with the rest of the ROI. The full simulator preserves this local correlation structure, with higher correlations concentrated among neighboring channels rather than distributed uniformly across the ROI and reduced correlation with reduced spatial overlap with the ROI. In contrast, the Jacobian-free simulator produces an overly homogeneous correlation pattern, indicating that it captures shared temporal dynamics but does not adequately preserve the spatial variation induced by the measurement geometry. The MNE AR model shows a mixture of positive and negative correlations without a clear relationship to channel distance or optode configuration.

For the surgical-skill assessment dataset, the experimental ΔHbO correlation matrix shows a similar spatial organization across channels over the left and right M1 regions (Figure 6). Channels within the same local motor region tend to be more strongly correlated, whereas correlations between more distant channel groups across motor regions are weaker. The full simulator preserves this block-like structure,

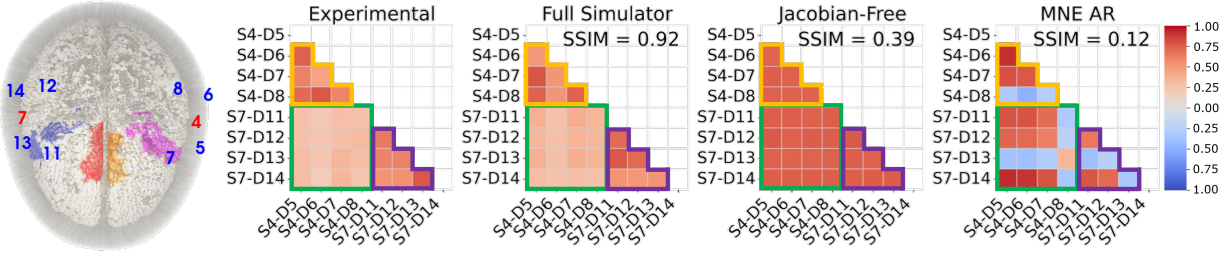


Figure 6: *Left*: Diagram of head mesh with active regions: left and right primary motor cortex (*pink* and *blue* regions of the brain) and left and right supplementary motor area (*orange* and *red*) along with relevant source (*red*) and detector (*blue*) positions on the surgical skill assessment montage (Figure 4). *Right*: Mean correlation matrices of ΔHbO for experimental surgical skill assessment, the proposed simulator, and benchmark models using channels above the left (*yellow*) and right primary motor cortex (*purple*) along with between-region correlations (*green*).

indicating that the sensitivity-matrix-based measurement model captures the spatial localization of the underlying hemodynamic responses. In contrast, the Jacobian-free simulator produces correlations that are too broadly elevated across channels, reducing the distinction between local and distant channel pairs. The MNE AR model again shows strong positive and negative correlations that do not follow the expected spatial organization of the optode geometry. Across both datasets, these results indicate that the full simulator better preserves localized hemodynamic structure, whereas the Jacobian-free and MNE AR baselines fail to reproduce the spatially graded cross-channel correlations observed experimentally.

4.3 Continuous Wavelet Transform

We further compare the spectral structure of the simulated and experimental short-separation channels using the continuous wavelet transform (CWT; Figure 7). Across both datasets, the simulated CWTs reproduce the dominant frequency structure observed experimentally, with pronounced activity in the low-frequency and cardiac bands and visible contributions in the respiratory range. This agreement is also reflected in the time-averaged CWT spectra, where the simulated and observed curves show almost identical peak locations and overall similar spectral profiles. For the finger-tapping dataset, the time-averaged simulated and experimental spectra show strong agreement across both wavelengths, with R^2 values of 0.93 and 0.90 for 690 and 830 nm, respectively. Notably, the relative power of cardiac activity is higher in the smaller wavelength λ_1 . This difference is not evident in the simulated data, suggesting that the systemic physiology scaling parameter ζ could be further tuned to more closely align simulated outcomes with the experimental data. Similarly high agreement in time-averaged CWT is observed for the surgical-skill assessment dataset, with R^2 values of 0.90 and 0.87 for λ_1 and λ_2 , respectively.

4.4 Global Summary Statistics

We next compare global summary statistics of the experimental and simulated signals (Figure 8; additional statistics in Figure A4). We consider the first four moments, minimum, maximum, range, and energy to assess whether the simulated signals fall within a plausible empirical range of signal scale, variability, and tail behavior. These descriptors are commonly used to characterize fNIRS responses across neurophotonic applications (Eser and Erdoğan, 2025; Lee et al., 2024; Wang et al., 2025; Eastmond et al., 2022).

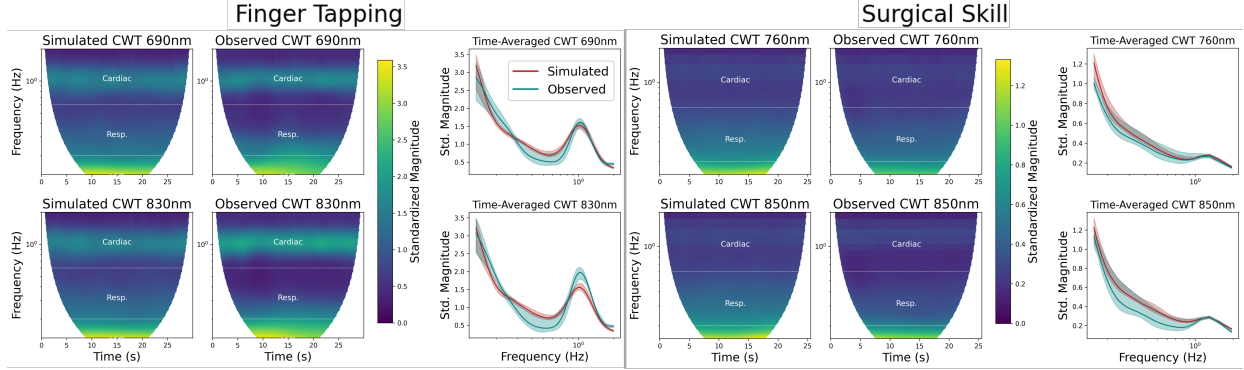


Figure 7: Comparison of continuous wavelet transforms (CWTs) for short-separation channels in the finger-tapping (*left*) and surgical-skill assessment (*right*) datasets. For each dataset and wavelength, simulated and experimentally observed CWTs are shown together with the corresponding time-averaged spectra. The simulated spectra (*red*) closely follow the experimentally observed spectra (*teal*), indicating that the simulator reproduces the dominant physiological frequency structure.

For the finger-tapping dataset, the full simulator with external artifacts provides the most consistent coverage of the empirical summary-statistic distributions. The means are well centered, and the extrema, standard deviations, range, energy, skewness, and kurtosis fall within a broadly comparable regime (Figure 8; Figure A4). Removing external artifacts substantially narrows the simulated distributions, especially for extrema, standard deviation, range, and energy. This supports the role of external artifacts in the full simulator in broadening signal variability, consistent with the correlation-based ablation results in Figure 5. The MNE AR baseline also captures aspects of the signal scale, as expected for a model fitted directly to experimental data, but it exhibits less consistent behavior across statistics, including a shifted mean and broader extrema.

For the surgical-skill assessment dataset, the simulated distributions are generally broader than for finger tapping, consistent with the larger HRF amplitudes used for this task (Table A4; Table A6). The full simulator again captures several central aspects of the empirical distributions, particularly the near-zero mean and plausible ranges for extrema and standard deviations. The Jacobian-free variants show stronger broadening in several scale- and tail-sensitive statistics, most visibly in maximum amplitude, skewness, kurtosis and range (Figure A4). Overall, these results show that the proposed simulator produces summary statistics in a realistic empirical range, while also confirming that global moments provide only a coarse validation of the simulated signal structure.

5 Discussion

Large-scale labeled fNIRS datasets are difficult to obtain, as experimental recordings are constrained by subject recruitment, task design, and measurement variability. This motivates the development of synthetic data generators that can produce controlled signals with known underlying sources and fully configurable nuisance components. In this paper, we introduced a simulation toolkit that combines the gold standard for modeling light transport through biological media Fang and Yan (2019) with a theory-driven model intended to capture known fNIRS signal contributions, including external artifacts (Brigadoi et al., 2014; Gao et al., 2022), systemic physiology (Hocke et al., 2018; Nguyen et al., 2018), and hemodynamic responses to cortical activity (Lindquist et al., 2009; Glover, 1999). By leveraging the Rytov approximation (O’Leary, 1996), we

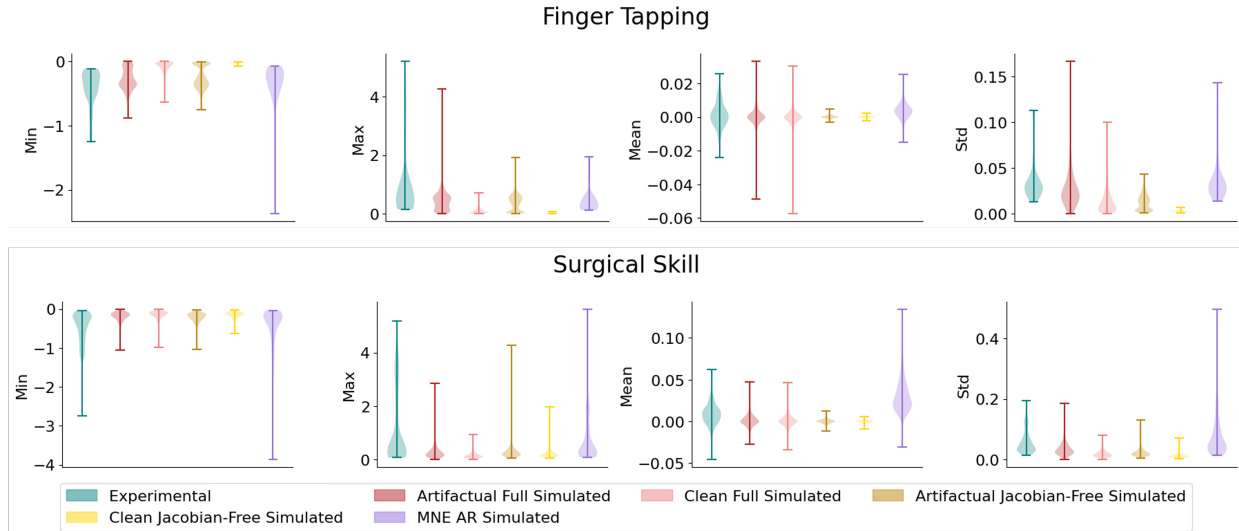


Figure 8: Global summary statistics for experimental and simulated fNIRS signals in the finger-tapping and surgical-skill assessment datasets. Violin plots compare the distributions of minimum, maximum, mean, and standard deviation across the experimental data, the full simulator with and without external artifacts, the Jacobian-free simulator with and without external artifacts, and the MNE AR baseline.

can efficiently and accurately map our simulated spatiotemporal changes in absorption to synthetic intensity measurements across the experimental probe (see [Appendix B](#)).

Across our initial validation experiments, the full (i.e., Jacobian-based) simulator captures several complementary properties of empirical fNIRS signals. The global summary statistics show that the simulated signals occupy a plausible range of amplitudes and variability, while the CWT analysis demonstrates that dominant physiological frequency components, including low-frequency and cardiac activity, are reproduced. At the same time, the cross-channel correlation analyses indicate that the simulator preserves spatially structured hemodynamic information across the probe. Thus, the main strength of the proposed model is its ability to jointly reproduce global signal scale, physiological spectral structure, and localized channel relationships.

The comparison with the Jacobian-free simulator highlights the importance of our sensitivity-aware measurement model. The Jacobian maps localized absorption changes in the head volume to probe-specific intensity measurements, preserving how cortical activity is expressed across nearby and distant channels. Without this sensitivity mapping, shared temporal components can still generate plausible time series and summary statistics, but the resulting channel correlations are not tied to the spatial organization of the probe. As seen in the experimental finger tapping correlation maps [Figure 5](#), not only are fNIRS signals sensitive to regions of interest, but also to the amount of overlap a channel has with an ROI, demonstrating decreased correlation in channels with reduced overlap with the ROI. Spatial sensitivity is especially important when multiple localized cortical activations must be represented, as in the surgical-skill assessment dataset [Figure A1](#).

The component ablations further show that the main simulator components contribute additively in physiologically interpretable ways. Systemic physiology introduces fluctuations shared across channels, whereas cortical hemodynamic responses remain localized around the activated region. External artifacts increase signal variability and widen the simulated distributions, improving agreement with several empirical summary statistics. The remaining differences are therefore best interpreted as sensitivity to dataset-specific

parameter choices that may require further hand-crafted tuning or model calibration.

Taken together, these comparisons clarify the trade-off between computational cost, fidelity, and mechanistic control. The Jacobian-free simulator provides a cheaper, low-fidelity alternative that can reproduce some global and temporal signal properties, but it is largely unsuitable for preserving spatially localized channel structure. The MNE AR baseline captures selected statistical features, as expected for a statistical model estimated directly from experimental recordings, but it does not provide explicit control over systemic physiology and external artifacts, or spatial localization of cortical activations. In contrast, our full simulator combines a physics-aware measurement model with interpretable signal components, making it suitable for generating controlled synthetic fNIRS data with both physiological and spatial structure.

Limitations Despite these promising results, our approach exhibits several limitations we plan to address in subsequent iterations. If the goal is to reproduce the characteristics of a particular experimental dataset, the simulator’s parameters currently require manual tuning. Improving fidelity therefore depends on prior knowledge of the noise, artifact, and physiological features present in the target data. In practice, this can lead either to overly broad parameter ranges that generate implausible signals or to time-consuming iterative adjustment to match dataset-specific structure. A natural next step is to estimate simulator parameters directly from experimental recordings using likelihood-free approaches such as simulation-based inference (SBI; [Cranmer et al., 2020](#)), enabling efficient calibration to a given dataset.

Another limitation on the fidelity of this work is the current reliance on a single head geometry. While perturbation-based approaches in Rytov and continuous-wave fNIRS may mitigate this weakness, further studies using other head meshes, such as those available in the ScatterBrains toolbox ([Wu et al., 2023](#)) could provide insight into the extent to which inter-subject variability affects our simulations.

Further, in this work, we instantiated the simulator using canonical double-gamma HRF basis functions. These parameterizations may be insufficient for longer-duration or quasi-continuous stimulation paradigms, where more flexible response models are often needed ([Lindquist et al., 2009](#)). Importantly, this is a limitation of the current instantiation rather than the general simulation framework. The simulator can incorporate alternative HRF parameterizations, including finite impulse response models and other flexible bases that can better capture sustained or non-canonical dynamics ([Lindquist et al., 2009](#)).

Finally, our current registration procedure aligns the montage to the head mesh without explicitly enforcing anatomical landmarks (fiducials) or physical constraints of the probe geometry. As a result, the fitted probe geometry can be unrealistically distorted to conform to the scalp surface, potentially altering source–detector separations and channel geometry in ways that would be infeasible in practice. Incorporating landmark-based constraints and simple mechanical priors (e.g., digital “springs” that penalize deviations from nominal inter-optode distances) would improve physical plausibility and reproducibility of registration across heads ([Aasted et al., 2015](#)).

6 Conclusion

We presented a spatiotemporally accurate, physiologically informed, full-head fNIRS simulator that combines mesh-based Monte Carlo photon transport with biophysically plausible models of cortical activation, systemic physiology, and external artifacts. By leveraging anatomically derived sensitivity matrices and the Rytov approximation, our simulator preserves probe-specific and wavelength-dependent spatiotemporal fidelity. Across two very different experimental paradigms, it reproduced key properties of empirical fNIRS data,

including physiological spectral peaks, cross-channel HRF correlation structure, and global signal statistics.

Looking ahead, automated parameter estimation, for example, through simulation-based inference, could enable dataset-specific calibration without manual tuning. Incorporating more flexible HRF models and subject-specific anatomical meshes would further improve realism in complex paradigms. Finally, extending the framework to multimodal settings, such as combined fNIRS–EEG or stimulation studies, could broaden its utility as a general-purpose toolkit for methodological validation and translational neuroimaging research.

7 Acknowledgments

This work was supported in part by NIH Grant No. F31EB035931 and NSF grant No. 2448380.

References

- Aarabi, A. and Huppert, T. J. (2016). Characterization of the relative contributions from systemic physiological noise to whole-brain resting-state functional near-infrared spectroscopy data using single-channel independent component analysis. *Neurophotonics*, 3(2):025004–025004.
- Aasted, C. M., Yücel, M. A., Cooper, R. J., Dubb, J., Tsuzuki, D., Becerra, L., Petkov, M. P., Borsook, D., Dan, I., and Boas, D. A. (2015). Anatomical guidance for functional near-infrared spectroscopy: Atlasviewer tutorial. *Neurophotonics*, 2(2):020801–020801.
- Barker, J. W., Aarabi, A., and Huppert, T. J. (2013). Autoregressive model based algorithm for correcting motion and serially correlated errors in fnirs. *Biomedical optics express*, 4(8):1366–1379.
- Besl, P. J. and McKay, N. D. (1992). Method for registration of 3-d shapes. In *Sensor fusion IV: control paradigms and data structures*, volume 1611, pages 586–606. Spie.
- Brigadoi, S., Ceccherini, L., Cutini, S., Scarpa, F., Scatturin, P., Selb, J., Gagnon, L., Boas, D. A., and Cooper, R. J. (2014). Motion artifacts in functional near-infrared spectroscopy: a comparison of motion correction techniques applied to real cognitive data. *Neuroimage*, 85:181–191.
- Chen, J. and Intes, X. (2011). Comparison of monte carlo methods for fluorescence molecular tomography—computational efficiency. *Medical physics*, 38(10):5788–5798.
- Cranmer, K., Brehmer, J., and Louppe, G. (2020). The frontier of simulation-based inference. *Proceedings of the National Academy of Sciences*, 117(48):30055–30062.
- Dehghani, H., Eames, M. E., Yalavarthy, P. K., Davis, S. C., Srinivasan, S., Carpenter, C. M., Pogue, B. W., and Paulsen, K. D. (2009). Near infrared optical tomography using nirfast: Algorithm for numerical model and image reconstruction. *Communications in numerical methods in engineering*, 25(6):711–732.
- Delpy, D. T., Cope, M., van der Zee, P., Arridge, S., Wray, S., and Wyatt, J. (1988). Estimation of optical pathlength through tissue from direct time of flight measurement. *Physics in Medicine & Biology*, 33(12):1433.
- Doherty, E. J., Spencer, C. A., Burnison, J., Čeko, M., Chin, J., Eloy, L., Haring, K., Kim, P., Pittman, D., Powers, S., et al. (2023). Interdisciplinary views of fnirs: Current advancements, equity challenges, and

- an agenda for future needs of a diverse fnirs research community. *Frontiers in integrative neuroscience*, 17:1059679.
- Donoghue, T., Haller, M., Peterson, E. J., Varma, P., Sebastian, P., Gao, R., Noto, T., Lara, A. H., Wallis, J. D., Knight, R. T., et al. (2020). Parameterizing neural power spectra into periodic and aperiodic components. *Nature neuroscience*, 23(12):1655–1665.
- Eastmond, C., Subedi, A., De, S., and Intes, X. (2022). Deep learning in fnirs: a review. *Neurophotonics*, 9(4):041411–041411.
- Eser, A. and Erdođan, S. B. (2025). Decoding basic emotional states through integration of an fnirs-based brain–computer interface with supervised learning algorithms. *Plos one*, 20(7):e0325850.
- Fang, Q. (2010). Mesh-based monte carlo method using fast ray-tracing in plücker coordinates. *Biomedical optics express*, 1(1):165–175.
- Fang, Q. and Boas, D. A. (2009). Monte carlo simulation of photon migration in 3d turbid media accelerated by graphics processing units. *Opt. Express*, 17(22):20178–20190.
- Fang, Q. and Yan, S. (2019). Graphics processing unit-accelerated mesh-based monte carlo photon transport simulations. *Journal of Biomedical Optics*, 24(11):115002–115002.
- Friston, K. J. (2003). Statistical parametric mapping. In *Neuroscience databases: a practical guide*, pages 237–250. Springer.
- Gao, L., Lin, Q., Tian, D., Zhu, S., and Tai, X. (2024). Advances and trends in the application of functional near-infrared spectroscopy for pediatric assessments: a bibliometric analysis. *Frontiers in Neurology*, 15:1459214.
- Gao, Y., Chao, H., Cavuoto, L., Yan, P., Kruger, U., Norfleet, J. E., Makled, B. A., Schwaitzberg, S., De, S., and Intes, X. (2022). Deep learning-based motion artifact removal in functional near-infrared spectroscopy. *Neurophotonics*, 9(4):041406–041406.
- Glover, G. H. (1999). Deconvolution of impulse response in event-related bold fmri. *Neuroimage*, 9(4):416–429.
- Goodfellow, I. J., Pouget-Abadie, J., Mirza, M., Xu, B., Warde-Farley, D., Ozair, S., Courville, A., and Bengio, Y. (2014). Generative adversarial nets. In Ghahramani, Z., Welling, M., Cortes, C., Lawrence, N., and Weinberger, K., editors, *Advances in Neural Information Processing Systems*, volume 27. Curran Associates, Inc.
- Hocke, L. M., Oni, I. K., Duszynski, C. C., Corrigan, A. V., Frederick, B. d., and Dunn, J. F. (2018). Automated processing of fnirs data—a visual guide to the pitfalls and consequences. *Algorithms*, 11(5):67.
- Holmes, C. J., Hoge, R., Collins, L., Woods, R., Toga, A. W., and Evans, A. C. (1998). Enhancement of mr images using registration for signal averaging. *Journal of computer assisted tomography*, 22(2):324–333.
- Huppert, T. J., Diamond, S. G., Franceschini, M. A., and Boas, D. A. (2009). Homer: a review of time-series analysis methods for near-infrared spectroscopy of the brain. *Applied optics*, 48(10):D280–D298.

- Jahani, S., Setarehdan, S. K., Boas, D. A., and Yücel, M. A. (2018). Motion artifact detection and correction in functional near-infrared spectroscopy: a new hybrid method based on spline interpolation method and savitzky–golay filtering. *Neurophotonics*, 5(1):015003–015003.
- Kamat, A., Eastmond, C., Gao, Y., Nemani, A., Yanik, E., Cavuoto, L., Hackett, M., Norfleet, J., Schwaitzberg, S., De, S., et al. (2023). Assessment of surgical tasks using neuroimaging dataset (astaund). *Scientific Data*, 10(1):699.
- Klein, F., Kohl, S. H., Lührs, M., Mehler, D. M., and Sorger, B. (2024). From lab to life: challenges and perspectives of fnirs for haemodynamic-based neurofeedback in real-world environments. *Philosophical Transactions B*, 379(1915):20230087.
- Leamy, D. J., Ward, T. E., and Sweeney, K. T. (2011). Functional near infrared spectroscopy (fnirs) synthetic data generation. In *2011 Annual International Conference of the IEEE Engineering in Medicine and Biology Society*, pages 6589–6592. IEEE.
- Lee, K., Kwon, J., Chun, M., Choi, J., Lee, S.-H., and Im, C.-H. (2024). Functional near-infrared spectroscopy-based computer-aided diagnosis of major depressive disorder using convolutional neural network with a new channel embedding layer considering inter-hemispheric asymmetry in prefrontal hemodynamic responses. *Depression and Anxiety*, 2024(1):4459867.
- Lewis, A. V. and Fang, Q. (2024). Revisiting equivalent optical properties for cerebrospinal fluid to improve diffusion-based modeling accuracy in the brain. *bioRxiv*.
- Lindquist, M. A., Loh, J. M., Atlas, L. Y., and Wager, T. D. (2009). Modeling the hemodynamic response function in fmri: efficiency, bias and mis-modeling. *Neuroimage*, 45(1):S187–S198.
- Liu, D., Zhang, Y., Zhang, P., Li, T., Li, Z., Zhang, L., and Gao, F. (2022). Deep-learning informed kalman filtering for priori-free and real-time hemodynamics extraction in functional near-infrared spectroscopy. *Biomedical optics express*, 13(9):4787–4801.
- Luke, R., Larson, E., Shader, M. J., Innes-Brown, H., Van Yper, L., Lee, A. K., Sowman, P. F., and McAlpine, D. (2021a). Analysis methods for measuring passive auditory fnirs responses generated by a block-design paradigm. *Neurophotonics*, 8(2):025008–025008.
- Luke, R., Shader, M. J., and McAlpine, D. (2021b). Characterization of mayer-wave oscillations in functional near-infrared spectroscopy using a physiologically informed model of the neural power spectra. *Neurophotonics*, 8(4):041001–041001.
- McDowell, K., Lin, C.-T., Oie, K. S., Jung, T.-P., Gordon, S., Whitaker, K. W., Li, S.-Y., Lu, S.-W., and Hairston, W. D. (2013). Real-world neuroimaging technologies. *Ieee Access*, 1:131–149.
- McSharry, P. E., Clifford, G. D., Tarassenko, L., and Smith, L. A. (2003). A dynamical model for generating synthetic electrocardiogram signals. *IEEE transactions on biomedical engineering*, 50(3):289–294.
- Middell, E., Carlton, L., Moradi, S., Codina, T., Fischer, T., Cutler, J., Kelley, S., Behrendt, J., Dissanayake, T., Harmening, N., et al. (2026). Cedalion tutorial: A python-based framework for comprehensive analysis of multimodal fnirs & dot from the lab to the everyday world. *arXiv preprint arXiv:2601.05923*.

- Nagasawa, T., Sato, T., Nambu, I., and Wada, Y. (2020). fnirs-gans: data augmentation using generative adversarial networks for classifying motor tasks from functional near-infrared spectroscopy. *Journal of Neural Engineering*, 17(1):016068.
- Naseer, N. and Hong, K.-S. (2015). fnirs-based brain-computer interfaces: a review. *Frontiers in human neuroscience*, 9:3.
- Nguyen, H.-D., Yoo, S.-H., Bhutta, M. R., and Hong, K.-S. (2018). Adaptive filtering of physiological noises in fnirs data. *Biomedical engineering online*, 17:1–23.
- Nizam, N. I., Ochoa, M., Smith, J. T., Gao, S., and Intes, X. (2022). Monte carlo-based data generation for efficient deep learning reconstruction of macroscopic diffuse optical tomography and topography applications. *Journal of Biomedical Optics*, 27(8):083016–083016.
- O’Leary, M. A. (1996). *Imaging with diffuse photon density waves*. PhD thesis, University of Pennsylvania.
- Pinti, P., Aichelburg, C., Gilbert, S., Hamilton, A., Hirsch, J., Burgess, P., and Tachtsidis, I. (2018). A review on the use of wearable functional near-infrared spectroscopy in naturalistic environments. *Japanese Psychological Research*, 60(4):347–373.
- Pinti, P., Scholkmann, F., Hamilton, A., Burgess, P., and Tachtsidis, I. (2019). Current status and issues regarding pre-processing of fnirs neuroimaging data: an investigation of diverse signal filtering methods within a general linear model framework. *Frontiers in human neuroscience*, 12:505.
- Pinti, P., Tachtsidis, I., Hamilton, A., Hirsch, J., Aichelburg, C., Gilbert, S., and Burgess, P. W. (2020). The present and future use of functional near-infrared spectroscopy (fnirs) for cognitive neuroscience. *Annals of the new York Academy of Sciences*, 1464(1):5–29.
- Pucci, O., Toronov, V., and St. Lawrence, K. (2010). Measurement of the optical properties of a two-layer model of the human head using broadband near-infrared spectroscopy. *Applied optics*, 49(32):6324–6332.
- Rahman, M. A., Siddik, A. B., Ghosh, T. K., Khanam, F., and Ahmad, M. (2020). A narrative review on clinical applications of fnirs. *Journal of Digital Imaging*, 33(5):1167–1184.
- Rasheed, K., Qadir, J., O’Brien, T. J., Kuhlmann, L., and Razi, A. (2021). A generative model to synthesize eeg data for epileptic seizure prediction. *IEEE Transactions on Neural Systems and Rehabilitation Engineering*, 29:2322–2332.
- Reddy, P., Izzetoglu, M., Shewokis, P. A., Sangobowale, M., Diaz-Arrastia, R., and Izzetoglu, K. (2021). Evaluation of fnirs signal components elicited by cognitive and hypercapnic stimuli. *Scientific reports*, 11(1):23457.
- Rolls, E. T., Huang, C.-C., Lin, C.-P., Feng, J., and Joliot, M. (2020). Automated anatomical labelling atlas 3. *Neuroimage*, 206:116189.
- Santosa, H., Zhai, X., Fishburn, F., and Huppert, T. (2018). The nirs brain analyzer toolbox. *Algorithms*, 11(5):73.
- Scholkmann, F., Kleiser, S., Metz, A. J., Zimmermann, R., Pavia, J. M., Wolf, U., and Wolf, M. (2014). A review on continuous wave functional near-infrared spectroscopy and imaging instrumentation and methodology. *Neuroimage*, 85:6–27.

- Strangman, G., Franceschini, M. A., and Boas, D. A. (2003). Factors affecting the accuracy of near-infrared spectroscopy concentration calculations for focal changes in oxygenation parameters. *Neuroimage*, 18(4):865–879.
- Tolley, N., Rodrigues, P. L., Gramfort, A., and Jones, S. R. (2024). Methods and considerations for estimating parameters in biophysically detailed neural models with simulation based inference. *PLOS Computational Biology*, 20(2):e1011108.
- Tran, A. P., Yan, S., and Fang, Q. (2020). Improving model-based functional near-infrared spectroscopy analysis using mesh-based anatomical and light-transport models. *Neurophotonics*, 7(1):015008–015008.
- Wang, Y., Zeng, W., Zou, L., Wang, Q., Ren, B., Xiong, Q., Bai, Y., and Feng, Z. (2025). Detecting cognitive motor dissociation by functional near-infrared spectroscopy. *Frontiers in Neurology*, 16:1532804.
- Wickramaratne, S. D. and Mahmud, M. S. (2021). Conditional-gan based data augmentation for deep learning task classifier improvement using fnirs data. *Frontiers in big Data*, 4:659146.
- Wray, S., Cope, M., Delpy, D. T., Wyatt, J. S., and Reynolds, E. O. R. (1988). Characterization of the near infrared absorption spectra of cytochrome aa3 and haemoglobin for the non-invasive monitoring of cerebral oxygenation. *Biochimica et Biophysica Acta (BBA)-Bioenergetics*, 933(1):184–192.
- Wu, M. M., Horstmeyer, R., and Carp, S. A. (2023). scatterbrains: an open database of human head models and companion optode locations for realistic monte carlo photon simulations. *Journal of biomedical optics*, 28(10):100501–100501.
- Yao, R., Intes, X., and Fang, Q. (2018). Direct approach to compute jacobians for diffuse optical tomography using perturbation monte carlo-based photon “replay”. *Biomedical optics express*, 9(10):4588–4603.
- Yaroslavsky, A., Schulze, P., Yaroslavsky, I., Schober, R., Ulrich, F., and Schwarzmaier, H. (2002). Optical properties of selected native and coagulated human brain tissues in vitro in the visible and near infrared spectral range. *Physics in Medicine & Biology*, 47(12):2059.
- Yücel, M. A., Aasted, C. M., Petkov, M. P., Borsook, D., Boas, D. A., and Becerra, L. (2015a). Specificity of hemodynamic brain responses to painful stimuli: a functional near-infrared spectroscopy study. *Scientific reports*, 5(1):9469.
- Yücel, M. A., Luke, R., Mesquita, R. C., von Lühmann, A., Mehler, D. M., Lühns, M., Gemignani, J., Abdalmalak, A., Albrecht, F., de Almeida Ivo, I., et al. (2025). fnirs reproducibility varies with data quality, analysis pipelines, and researcher experience. *Communications biology*, 8(1):1149.
- Yücel, M. A., Selb, J., Aasted, C. M., Petkov, M. P., Becerra, L., Borsook, D., and Boas, D. A. (2015b). Short separation regression improves statistical significance and better localizes the hemodynamic response obtained by near-infrared spectroscopy for tasks with differing autonomic responses. *Neurophotonics*, 2(3):035005–035005.
- Zimeo Morais, G. A., Balardin, J. B., and Sato, J. R. (2018). fnirs optodes’ location decider (fold): a toolbox for probe arrangement guided by brain regions-of-interest. *Scientific reports*, 8(1):1–11.

A Additional results

A.1 Pain Assessment Experiment

A.1.1 Experimental setting

In addition to the finger tapping recordings, the dataset described in [Yücel et al. \(2015b\)](#) includes an electrical stimulus pain assessment experiment, which uses the same subjects, fNIRS spectrometer, and optode montage. This study used a 5 Hz electrical stimulator (Neurometer CPT, Neurotron, Baltimore, Maryland), which was attached to the left thumb of each subject. Prior to the start of the recording, subjects had the electrical stimulator calibrated to determine subjective pain ratings of 3/10 (innocuous) and 7/10 (noxious). After the finger tapping task recording described in [Section 3.1](#), subjects underwent the pain assessment task, with 5 s of electrical stimulus followed by 25 s of rest. Each recording consisted of 12 noxious and 12 innocuous stimuli, randomly ordered, for a total of 12.5 minutes each run.

A.1.2 Pain assessment results

Cortical activity analysis In the analysis of the pain assessment dataset, a broad ROI across the montage was selected, covering the left and right somatosensory regions and the prefrontal cortex. In the mean correlation matrices [Figure A1](#), we continue to see a similar trend: the MNE AR model and the Jacobian-free model do not encode spatial information (SSIMs of 0.26 and 0.74, respectively). Comparatively, in the full simulator and experimental data, we can see a slightly higher correlation across the prefrontal cortex channels when compared to the experimental data, but no further comparable features are observed between the full model and the experimental data (SSIM of 0.64), suggesting the model parameters may be further tuned to improve accuracy.

Spectral analysis Similar to the results shown in [Section 4](#), with the finger tapping and surgical skill assessment dataset, we see clear peaks in the low frequency and cardiac peaks in both the experimentally observed and simulated data, resulting in R^2 scores of 0.90 and 0.91 for the 690 and 830 nm wavelengths, respectively ([Figure A2](#)).

Summary statistics When comparing the summary statistics for the experimental pain assessment dataset with those of the benchmark models ([Figure A3](#)), there is observable overdispersion in kurtosis in the simulated data with motion artifacts. Aside from this, the proposed simulator with motion artifacts demonstrates comparable, though not identical, distributions across all other summary statistics.

A.2 Summary Statistics

In addition to the statistics provided in [Figure 8](#), we present four additional statistics shown in [Figure A4](#) commonly used for the analysis of fNIRS data ([Eser and Erdoğan, 2025](#); [Lee et al., 2024](#); [Wang et al., 2025](#); [Eastmond et al., 2022](#)). Summary statistics results for the pain assessment task are shown in [Figure A3](#) and are discussed in the appendix section above.

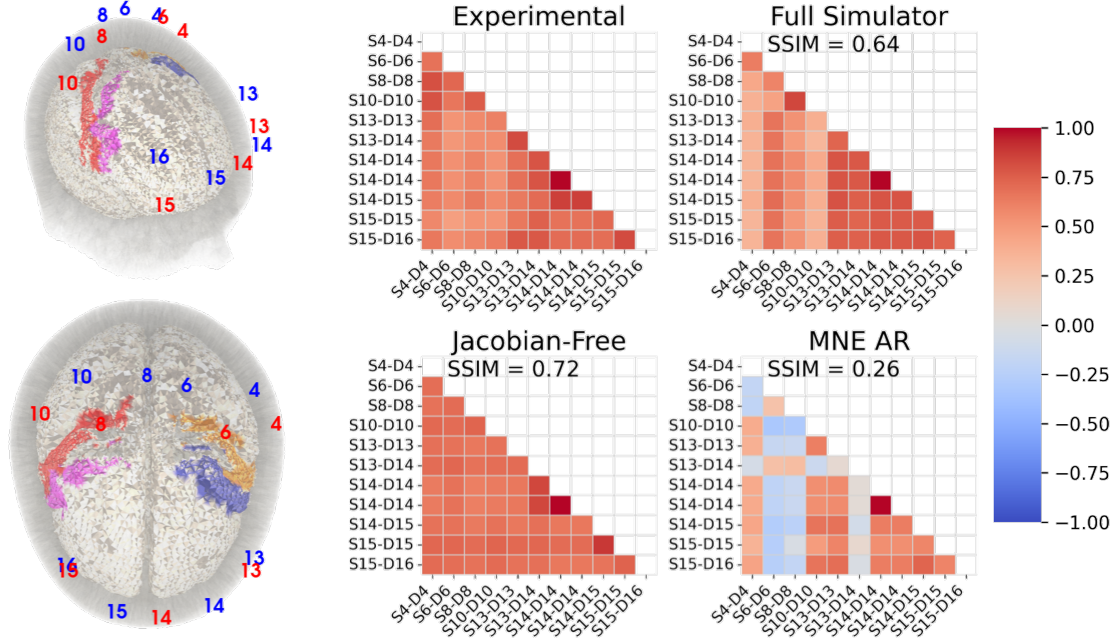


Figure A1: Diagram of the spatial activation and relevant source and detector locations (*top*) along with mean correlation matrices of the HRF in the left and right somatosensory cortex (orange and red) for the experimental pain assessment data, our Jacobian-enabled simulation approach, Jacobian-free simulations, and MNE-AR simulations using the denoising pipeline described in Section 3.2 (*bottom*).

A.3 MNE AR CWT

Here, we present the CWT for the MNE AR model and compare it with the experimental finger-tapping and surgical skill assessment datasets (Figure A5). Unlike our proposed model, the CWT of the MNE AR model does not capture the cardiac peak present in either experimental dataset; instead, it broadly follows a $1/f$ exponential curve.

A.4 FOOOF Spectral Analysis

Due to the mean CWT plots showing an aggregate of the spectra, here we use the spectral parameterization tool from the FOOOF toolbox (Donoghue et al., 2020) to estimate the systemic physiology peaks found in the PSD of each signal. Here we take an example short separation channel from each simulated and experimental trial, and plot the peaks detected by the FOOOF algorithm in each frequency band of interest. The distribution of the simulated data from our full simulator with artifacts and the MNE AR model are plotted as ellipses centered on the mean of the peaks within that band and a radius that corresponds to three standard deviations of the data. We then plot the estimated peaks from the experimental data and calculate how many of the experimental peaks fall within the ellipse for each simulator. Due to the surgical skill assessment data having a lower sampling rate and being cropped to the shortest signal length, the frequency resolution is insufficient for detecting peaks using the FOOOF algorithm.

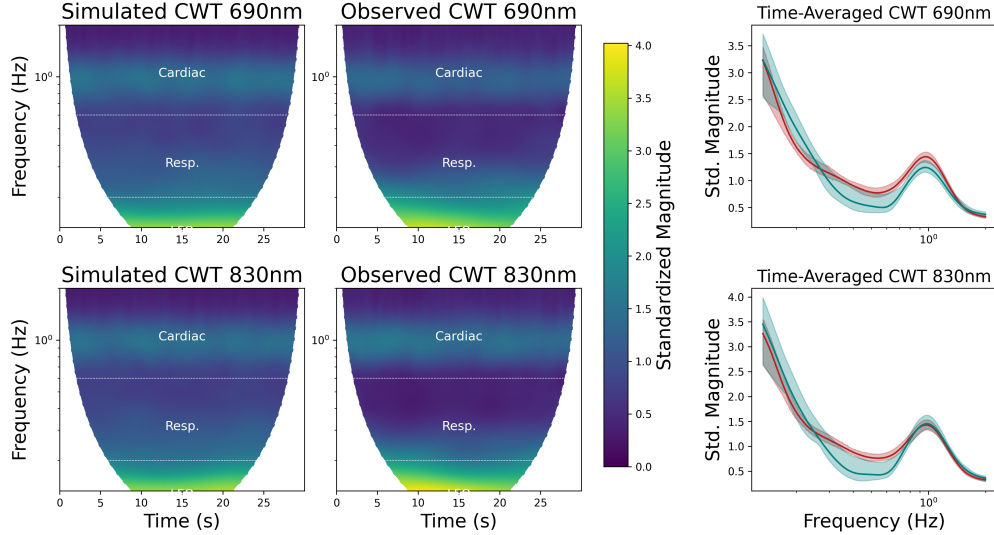


Figure A2: A comparison of the continuous wavelet transform of the short separation channels between the simulated Jacobian-enabled data and the experimental data for the pain assessment dataset, along with the corresponding time-averaged CWT for the simulated (*red*) and experimental (*teal*) data.

A.4.1 FOOF Results

Broadly, we can see that our simulator captures the majority of the peaks across all frequency bands in the finger tapping dataset [Table A1](#). Comparatively, the MNE AR model demonstrates a comparably high performance across the LFO and respiratory frequency bands, but performs far worse in the cardiac frequency bands. Notably, this is due to the MNE AR model consistently underestimating the power in the cardiac band peaks of the experimental data [Figure A6](#), capturing almost none of the cardiac peaks present at the 830nm wavelength. In the pain assessment dataset, our full simulator demonstrates lower performance in the LFO frequency band [Table A1](#). In the LFO region, our proposed simulator does not capture the peaks at the extreme low end of the LFO frequency band [Figure A7](#), suggesting that parameters such as ρ or α_1 could be further tuned. In all other frequency bands, our proposed simulator performs comparably to the finger tapping dataset, with a consistently high percentage of experimental peaks being captured in both the respiratory and cardiac peaks. The MNE AR dataset similarly performs comparably to the finger tapping data in the respiratory and cardiac peaks, capturing nearly all of the peaks in the respiratory band and few of the cardiac peaks, particularly at 830 nm. In the LFO frequency band the MNE AR simulator sees a drop in performance at the 830 nm wavelength, demonstrating a slight underestimation of relative power in this frequency band. In general, we see that our proposed simulator is capable of broadly capturing the majority of the peaks across both datasets and all relevant frequency bands, while the MNE AR model greatly underperforms in capturing the cardiac frequency band peaks.

B Simulator details

B.1 Mesh-Based Monte Carlo Simulations

Using the command line interface of MMC V2025.10 (Bubble Tea), each optode is simulated via the simulation parameters listed in [Table A2](#) and the relevant optical properties listed in [Table A3](#). With the given

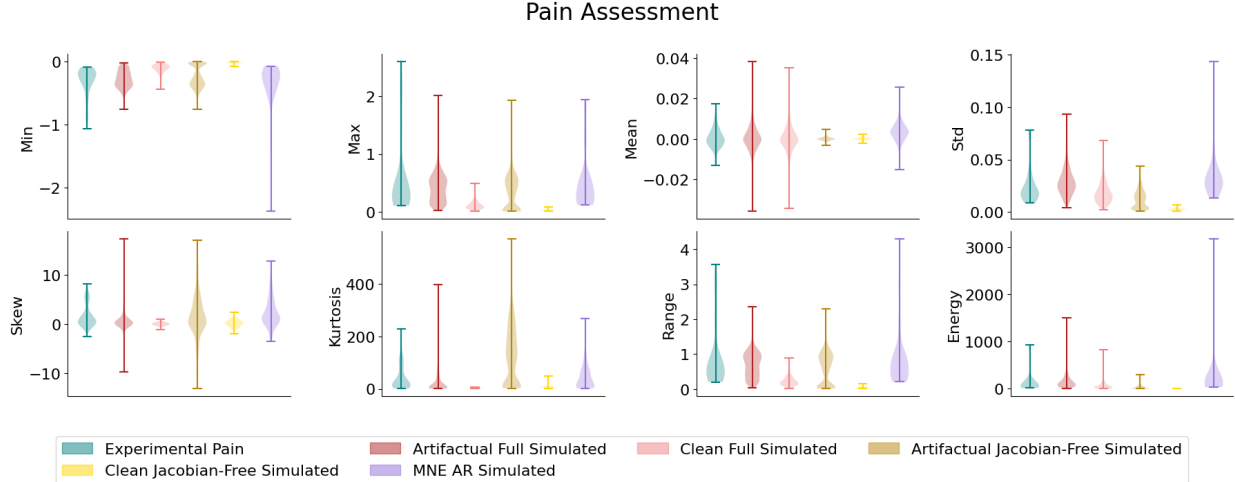


Figure A3: A comparison of global summary statistics for experimental pain assessment data (*teal*), Jacobian-enabled synthetic data with external artifacts (*red*), without external artifacts (*pink*), Jacobian-free synthetic data with (*dark goldenrod*) and without motion artifacts (*yellow*), and the MNE AR simulated data (*purple*).

	Ours		MNE-AR	
	Finger Tapping	Pain	Finger Tapping	Pain
LFO 690 nm	0.84	0.77	0.97	0.90
Respiratory 690 nm	1.0	1.0	1.0	1.0
Cardiac 690 nm	0.99	0.93	0.50	0.49
LFO 830 nm	0.93	0.77	0.89	0.78
Respiratory 830 nm	1.0	1.0	0.9	0.96
Cardiac 830 nm	1.0	1.0	0.08	0.11

Table A1: Percentage of systemic physiology peaks captured by ellipse of simulation peaks (3 standard deviations in each axis)

input parameters it takes roughly 30 minutes on an NVIDIA GeForce RTX 3090 to simulate each optode using MMC.

B.2 Simulation Settings for Finger Tapping and Pain Datasets

Pain and finger-tapping data are simulated using 30-second trials with a stimulus onset of 5 seconds, a stimulus duration of 5 seconds, and a post-stimulus rest of 20 seconds, corresponding to the experimental protocol. All model hyperparameters used to simulate the finger-tapping and pain assessment datasets are listed in Table A4 and Table A5, respectively. An example simulated finger-tapping trial is shown in Figure A8, using parameters sampled from Table A4. In terms of computational efficiency, on an 11th Gen Intel Core i9-11900K, we simulate 1000 30-second finger-tapping trials in ≈ 53 minutes for Jacobian-informed simulations and < 1 minute for Jacobian-free simulations. These simulation speeds do not include time for Jacobian generation. In comparison, the MNE AR simulator takes ≈ 185 minutes to generate 100 finger tapping trials.

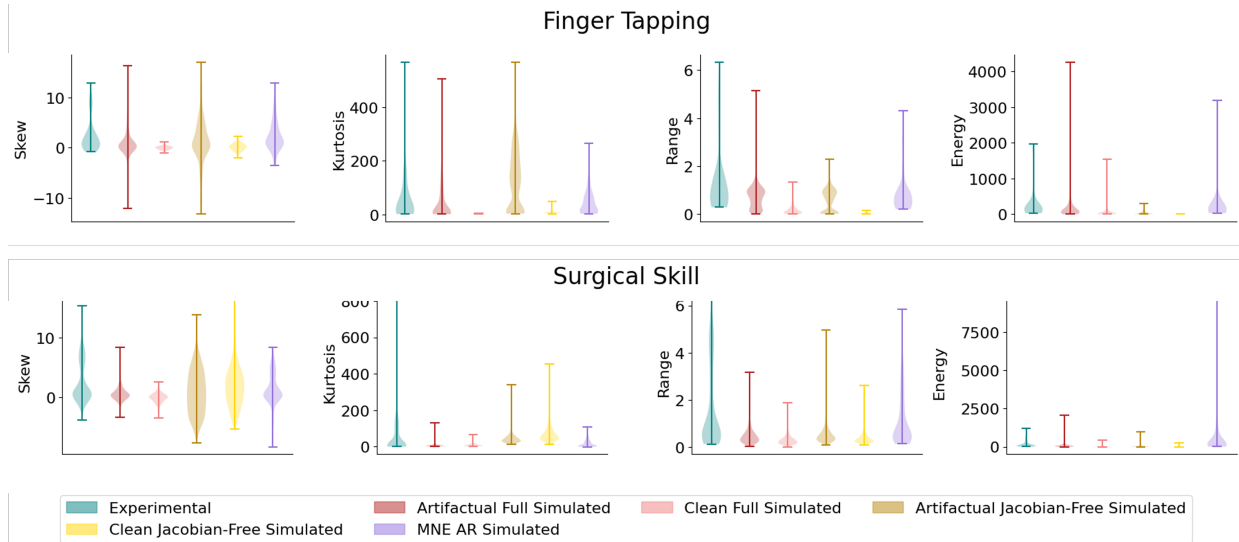


Figure A4: Additional global summary statistics for experimental and simulated fNIRS signals in the finger-tapping and surgical-skill assessment datasets. Violin plots show skewness, kurtosis, range, and signal energy. These statistics are more sensitive to tail behavior and rare high-amplitude events than the first-order statistics shown in Figure 8.

Parameter	Value	Description
nphoton	5e9	Number of simulated photons
tstart	0	Simulation starting time
tend	5e-9	Simulation ending time
tstep	5e-9	Duration of simulation time step
method	elem	Ray-tracing method
issaveexit	1	Option to save photon exit positions and directions
issavedet	1	Option to save photon info at detectors
outputtype	flux	Output quantity

Table A2: Input parameters for MMC simulations.

B.3 Simulation Settings for Surgical Skill Dataset

Pain and finger tapping data are simulated via 30-second trials with a stimulus start uniformly sampled from a range of 0 to 20 seconds, stimulus duration uniformly sampled from a range of 30-98 seconds, and a post-stimulus rest time uniformly sampled from a range of 0 to 30 seconds, which is consistent with the recorded trial start and end times present in the experimental data. All model hyperparameters used to simulate this dataset are listed in Table A6. An example simulation of a surgical skill trial is shown in Figure A9 using parameters sampled from Table A6. In terms of computational efficiency, on an 11th Gen Intel Core i9-11900K, we simulate 1000 30-98-second trials of surgical skill assessment data in ≈ 15 minutes for Jacobian-informed simulations and < 1 minute for Jacobian-free simulations. These simulation speeds do not include time for Jacobian generation. In comparison, the MNE AR simulator takes ≈ 68 minutes to generate 500 trials of surgical skill assessment data.

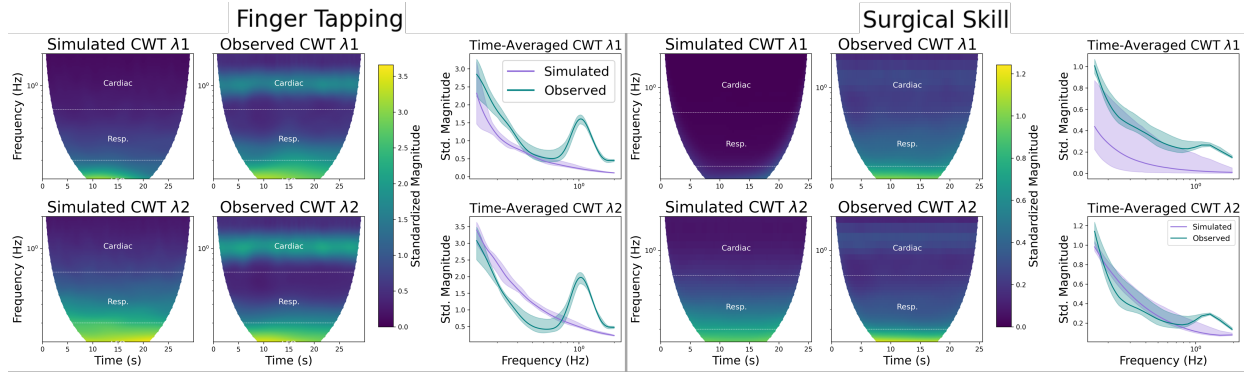


Figure A5: A comparison of the continuous wavelet transform of the short separation channels between the simulated Jacobian-enabled data and the experimental data for the finger tapping (*left*) and surgical skill assessment (*right*) datasets, along with the corresponding time-averaged CWT for the MNE AR simulated (*purple*) and experimental (*teal*) data.

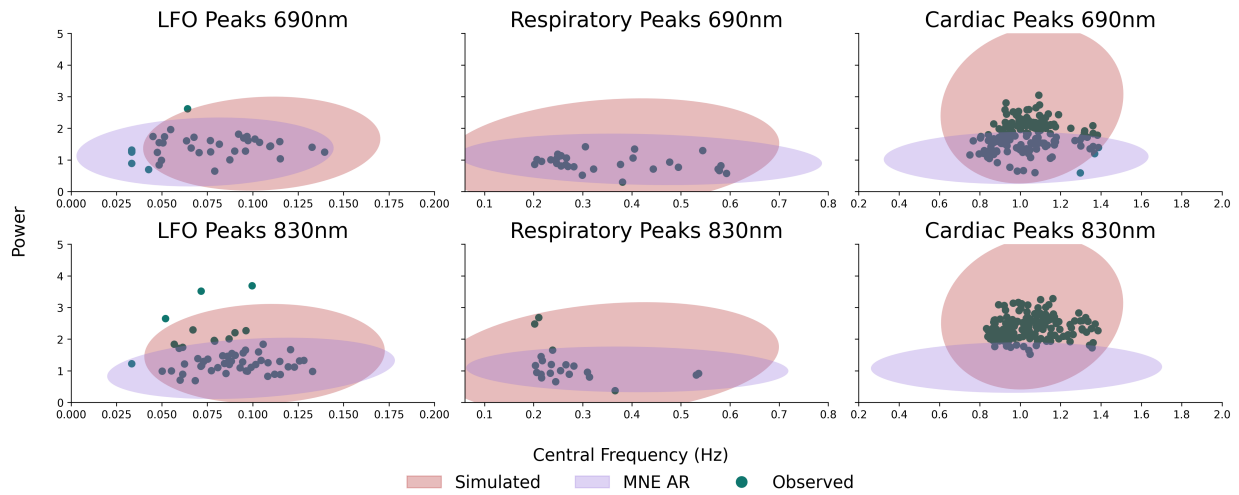


Figure A6: Spectral peaks captured by the FOOOF algorithm (Donoghue et al., 2020) in the frequency bands of interest (LFO, respiratory, cardiac) in the experimental data (teal), full simulator (red) and MNE AR simulator (purple) for the finger tapping dataset.

C Code availability

The code associated with this manuscript will be made public upon publication.

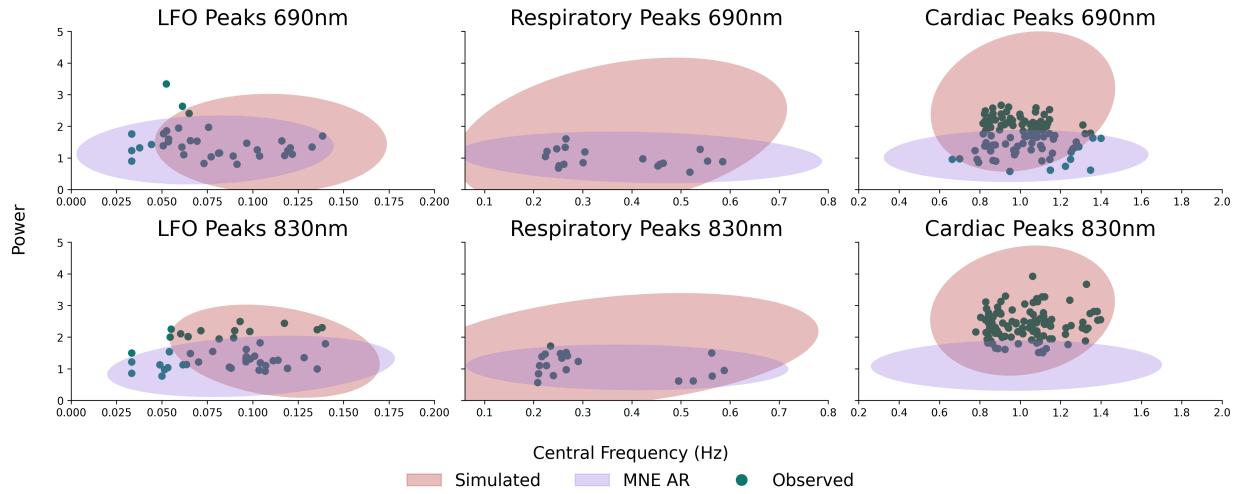


Figure A7: Spectral peaks captured by the FOOOF algorithm (Donoghue et al., 2020) in the frequency bands of interest (LFO, respiratory, cardiac) in the experimental data (teal), full simulator (red) and MNE AR simulator (purple) for the pain assessment dataset.

Wavelength [nm]	Tissue Types	μ_a [mm^{-1}]	μ_s [mm^{-1}]	m	g	Reference
690/830	Scalp	.0159/.0191	.800/.660	1.4	.9	Strangman et al. (2003)
	Skull	.0101/.0136	1.00/.860	1.4	.9	Strangman et al. (2003)
	Cerebrospinal fluid	.0004/.0026	.010/.010	1.4	.9	Lewis and Fang (2024)
	Gray Matter	.0200/.0300	8.80/7.00	1.4	.9	Lewis and Fang (2024)
	White Matter	.0700/.0900	60.0/42.9	1.4	.9	Lewis and Fang (2024)
760/850	Scalp	.0220/.0220	8.20/7.50	1.4	.9	Pucci et al. (2010)
	Skull	.0125/.0136	.930/.860	1.4	.9	Strangman et al. (2003)
	Cerebrospinal fluid	.0021/.0026	.010/.010	1.4	.9	Strangman et al. (2003)
	Gray Matter	.0200/.0350	8.00/7.50	1.4	.9	Yaroslavsky et al. (2002)
	White Matter	.0800/.0800	40.0/34.2	1.4	.9	Yaroslavsky et al. (2002)

Table A3: Values of the optical properties for the different tissue types used in the simulations. Two different sets of wavelengths are used for the two experimental protocols. μ_a : absorption coefficient, μ_s : scattering coefficient, m : refractive index, g : anisotropy factor.

Parameter Symbol	Priors	Description
$\omega = (\omega_1, \dots, \omega_L)$	$\mathcal{U}(1.6, 3.3)$	Widths of Hemodynamic Response Functions.
$\tau = (\tau_1, \dots, \tau_L)$	$\mathcal{U}(4, 10)$	Times from onset of stimulus to peak of HRF.
$\kappa = (\kappa_1, \dots, \kappa_L)$	Expon($4.69e - 6$)	Magnitude of HRF peaks.
$\xi = (\xi_1, \dots, \xi_L)$	$\mathcal{U}(0.67, 0.75)$	Relative magnitude of concentration change of HbO to HbR.
η	$\mathcal{U}(0.01, 0.1)$	Constant signal offset in PSD; can be thought of as a global white noise contribution.
$\zeta = (\zeta_1, \zeta_2)$	45, 15	Scaling factor of systemic physiology time series signal to cortical activity contributions for each wavelength.
$\alpha = (\alpha_1, \alpha_2, \alpha_3)$	Dirichlet(7.0, 0.0625, 1.75) (Mayer waves, Respiratory, Cardiac)	Relative amplitude of Gaussian pulse to all systemic physiological contributions in the power spectral density; each α models an individual systemic physiological contribution to fNIRS signals.
$\nu = (\nu_1, \nu_2, \nu_3)$	$\mathcal{N}(\mu_1 = 0.1, \sigma_1 = 0.025)$ (Mayer Waves) $\mathcal{N}(\mu_1 = 0.3, \sigma_1 = 0.05)$ (Respiratory) $\mathcal{N}(\mu_1 = 1.07, \sigma_1 = 0.15)$ (Cardiac)	Central frequency of Gaussian pulses in the power spectral density; each ν models an individual systemic physiological contribution to fNIRS signals.
ρ	$\mathcal{N}(\mu_1 = 2.0, \sigma_1 = 0.1)$	Slope of the aperiodic $1/f^\rho$ exponential frequency component in the power spectral density.
$P(t_s)$	0.05	Probability (Bernoulli) of a spike artifact occurring at any second in a given time series
A_s	$\mathcal{U}(-2, 2)$	Amplitude of spike artifacts relative to the standard deviation of a given time series
$P(t_b)$	$P(t_b t_s) = 0.5$ $P(t_b t'_s) = 0.05$	Probability of a baseline shift artifact occurring at any second in a given time series ($P(t_b t'_s)$) or when a spike artifact is present ($P(t_b t_s)$)
A_b	$\mathcal{U}(-2, 2)$	Amplitude of baseline shift artifacts relative to the standard deviation of a given time series
ϵ	125	Minimum intensity value of time series resulting from addition of motion artifacts
$P(d)$	$\mathcal{U}(0, 0.025)$	Probability of channel dropout occurring in each channel
A_d	$\mathcal{U}(0.05, 0.15)$	Amplitude of Gaussian white noise relative to the standard deviation of a given time series
u_d	20	Minimum intensity value of time series resulting from channel dropout

Table A4: Full description of the simulation parameters used to generate synthetic *finger tapping* data. L denotes the number of active regions.

Parameter Symbol	Priors	Description
$\omega = (\omega_1, \dots, \omega_L)$	$\mathcal{U}(1.6, 3.3)$	Widths of Hemodynamic Response Functions.
$\tau = (\tau_1, \dots, \tau_L)$	$\mathcal{U}(4, 10)$	Times from onset of stimulus to peak of HRF.
$\kappa = (\kappa_1, \dots, \kappa_L)$	$\text{Expon}(5.04e - 7)$	Magnitude of HRF peaks.
$\xi = (\xi_1, \dots, \xi_L)$	$\mathcal{U}(0.67, 0.75)$	Relative magnitude of concentration change of HbO to HbR.
η	$\mathcal{U}(0.01, 0.1)$	Constant signal offset in PSD; can be thought of as a global white noise contribution.
$\zeta = (\zeta_1, \zeta_2)$	30, 15	Scaling factor of systemic physiology time series signal to cortical activity contributions for each wavelength.
$\alpha = (\alpha_1, \alpha_2, \alpha_3)$	Dirichlet(7.0, 0.0625, 1.5) (Mayer waves, Respiratory, Cardiac)	Relative amplitude of Gaussian pulse to all systemic physiological contributions in the power spectral density; each α models an individual systemic physiological contribution to fNIRS signals.
$\nu = (\nu_1, \nu_2, \nu_3)$	$\mathcal{N}(\mu_1 = 0.1, \sigma_1 = 0.025)$ (Mayer Waves) $\mathcal{N}(\mu_1 = 0.3, \sigma_1 = 0.05)$ (Respiratory) $\mathcal{N}(\mu_1 = 1.0, \sigma_1 = 0.15)$ (Cardiac)	Central frequency of Gaussian pulses in the power spectral density; each ν models an individual systemic physiological contribution to fNIRS signals.
ρ	$\mathcal{N}(\mu_1 = 2.0, \sigma_1 = 0.1)$	Slope of the aperiodic $1/f^\rho$ exponential frequency component in the power spectral density.
$P(t_s)$	0.02	Probability (Bernoulli) of a spike artifact occurring at any second in a given time series
A_s	$\mathcal{U}(-1.5, 1.5)$	Amplitude of spike artifacts relative to the standard deviation of a given time series
$P(t_b)$	$P(t_b t_s) = 0.5$ $P(t_b t'_s) = 0.02$	Probability of a baseline shift artifact occurring at any second in a given time series ($P(t_b t'_s)$) or when a spike artifact is present ($P(t_b t_s)$)
A_b	$\mathcal{U}(-1.5, 1.5)$	Amplitude of baseline shift artifacts relative to the standard deviation of a given time series
ϵ	125	Minimum intensity value of time series resulting from addition of motion artifacts
$P(d)$	$\mathcal{U}(0, 0.025)$	Probability of channel dropout occurring in each channel
A_d	$\mathcal{U}(0.05, 0.15)$	Amplitude of Gaussian white noise relative to the standard deviation of a given time series
ϵ_d	20	Minimum intensity value of time series resulting from channel dropout

Table A5: Full description of the simulation parameters used to generate synthetic *pain assessment* data. L denotes the number of active regions.

Parameter Symbol	Values	Description
$\omega = (\omega_1, \dots, \omega_L)$	$\mathcal{U}(1.6, 3.3)$	Widths of Hemodynamic Response Functions.
$\tau = (\tau_1, \dots, \tau_L)$	$\mathcal{U}(4, 10)$	Times from onset of stimulus to peak of HRF.
$\kappa = (\kappa_1, \dots, \kappa_L)$	$\text{Expon}(1.008e - 5)$	Magnitude of HRF peaks.
$\xi = (\xi_1, \dots, \xi_L)$	$\mathcal{U}(0.5, 0.6)$	Relative magnitude of concentration change of HbO to HbR.
η	$\mathcal{U}(0.01, 0.1)$	Constant signal offset in PSD; can be thought of as a global white noise contribution.
$\zeta = (\zeta_1, \zeta_2)$	10, 30	Scaling factor of systemic physiology time series signal to cortical activity contributions for each wavelength.
$\alpha = (\alpha_1, \alpha_2, \alpha_3)$	Dirichlet(7.0, 0.05, 0.25) (Mayer waves, Respiratory, Cardiac)	Relative amplitude of Gaussian pulse to all systemic physiological contributions in the power spectral density; each α models an individual systemic physiological contribution to fNIRS signals.
$\nu = (\nu_1, \nu_2, \nu_3)$	$\mathcal{N}(\mu_1 = 0.1, \sigma_1 = 0.025)$ (Mayer Waves) $\mathcal{N}(\mu_1 = 0.4, \sigma_1 = 0.05)$ (Respiratory) $\mathcal{N}(\mu_1 = 1.3, \sigma_1 = 0.15)$ (Cardiac)	Central frequency of Gaussian pulses in the power spectral density; each ν models an individual systemic physiological contribution to fNIRS signals.
ρ	$\mathcal{N}(\mu_1 = 2.0, \sigma_1 = 0.1)$	Slope of the aperiodic $1/f^\rho$ exponential frequency component in the power spectral density.
$P(t_s)$	0.05	Probability (Bernoulli) of a spike artifact occurring at any second in a given time series
A_s	$\mathcal{U}(-2, 2)$	Amplitude of spike artifacts relative to the standard deviation of a given time series
$P(t_b)$	$P(t_b t_s) = 0.5$ $P(t_b t'_s) = 0.05$	Probability of a baseline shift artifact occurring at any second in a given time series ($P(t_b t'_s)$) or when a spike artifact is present ($P(t_b t_s)$)
A_b	$\mathcal{U}(-2, 2)$	Amplitude of baseline shift artifacts relative to the standard deviation of a given time series
ϵ	20	Minimum intensity value of time series resulting from addition of motion artifacts
$P(d)$	0	Probability of channel dropout occurring in each channel
A_d	$\mathcal{U}(0.15, 0.25)$	Amplitude of Gaussian white noise relative to the standard deviation of a given time series
ϵ_d	15	Minimum intensity value of time series resulting from channel dropout

Table A6: Full description of the simulation parameters used to generate synthetic *surgical skill assessment* data. L denotes the number of active regions.

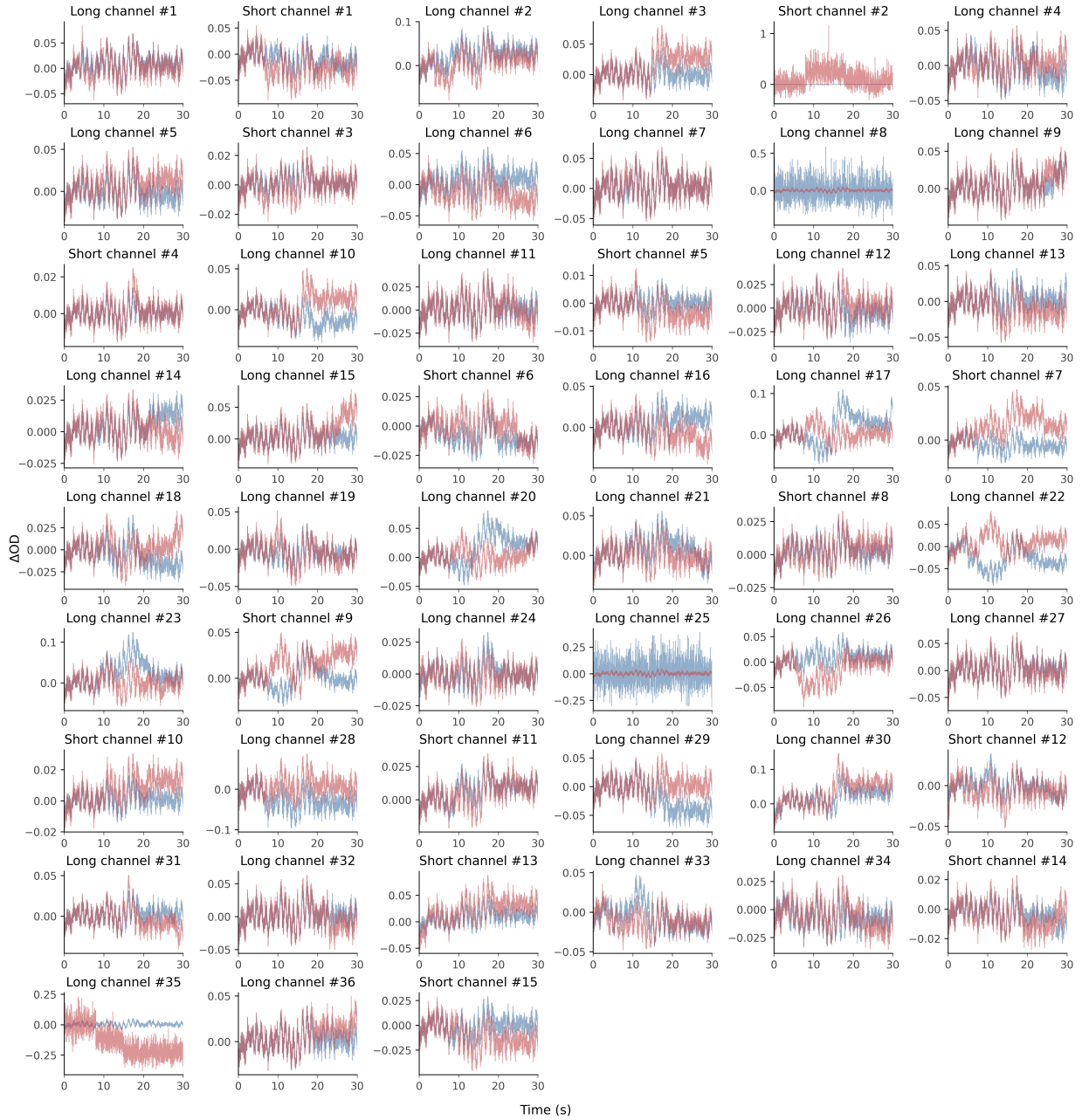


Figure A8: Example *full finger tapping simulator output*, of multi-channel fNIRS optical density in two wavelengths (λ_1 =blue, λ_2 =red), with long separation and short separation channels corresponding to the montage used for finger tapping and pain simulations and shown in [Figure 4](#).

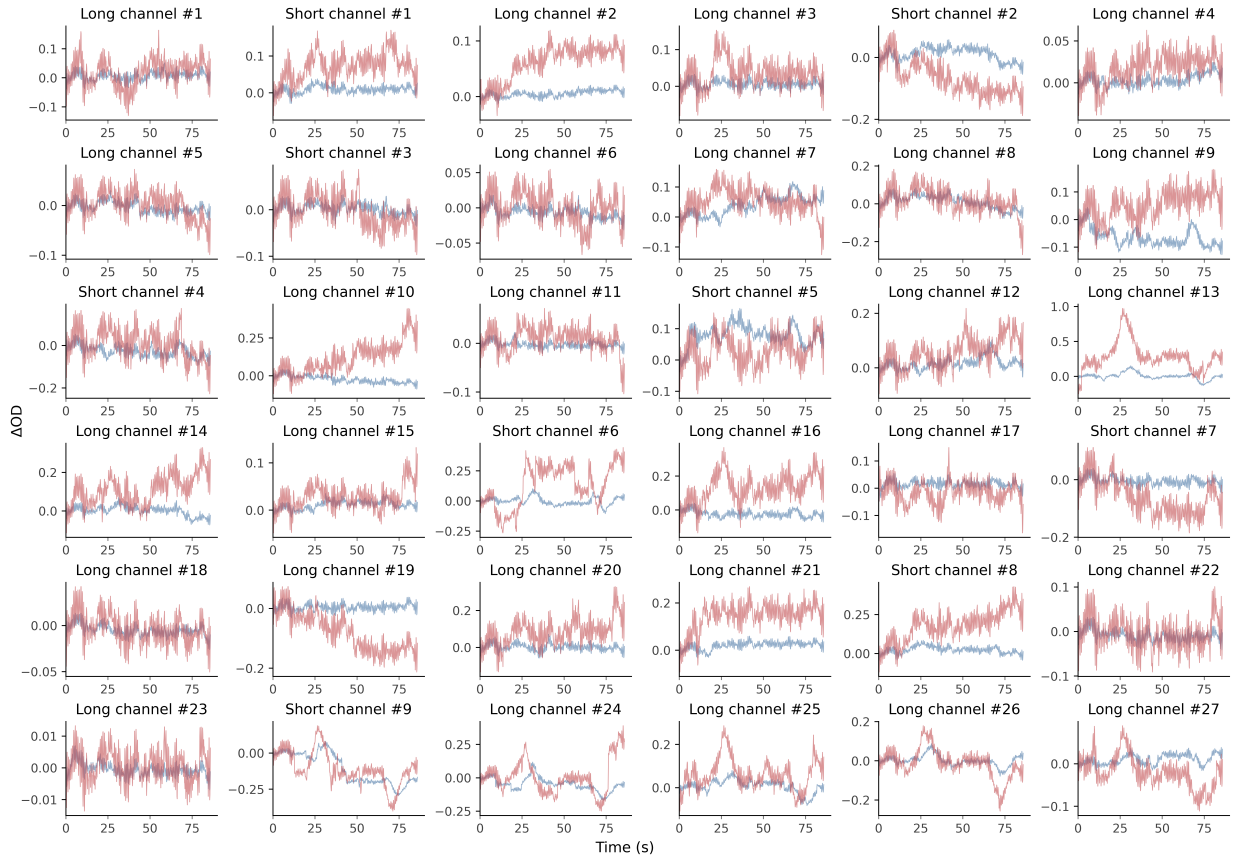


Figure A9: Example full simulator output for the *surgical skill assessment* setting, of multi-channel fNIRS optical density in two wavelengths (λ_1 =blue, λ_2 =red), with long separation and short separation channels corresponding to the montage shown in Figure 4.